

Linear response of rotating and flattened stellar clusters: the oblate Kuzmin–Kutuzov Stäckel family.

KERWANN TEP ^{1,2} CHRISTOPHE PICHON ^{2,3,4} AND MICHAEL S. PETERSEN ⁵

¹*Department of Physics and Astronomy, University of North Carolina at Chapel Hill, 120 E. Cameron Ave, Chapel Hill, NC, 27599, USA*

²*Institut d'Astrophysique de Paris, CNRS and Sorbonne Université, UMR 7095, 98 bis Boulevard Arago, F-75014 Paris, France*

³*IPhT, DRF-INP, UMR 3680, CEA, L'Orme des Merisiers, Bât 774, 91191 Gif-sur-Yvette, France*

⁴*Korea Institute for Advanced Study, 85 Hoegi-ro, Dongdaemun-gu, Seoul 02455, Republic of Korea*

⁵*Institute for Astronomy, University of Edinburgh, Royal Observatory, Blackford Hill, Edinburgh EH9 3HJ, UK*

ABSTRACT

This paper investigates the linear response of a series of spheroidal stellar clusters, the Kuzmin–Kutuzov Stäckel family, which exhibit a continuous range of flattening and rotation, extending from an isochrone sphere to a Toomre disk. The method successfully replicates the growing modes previously identified in published N -body simulations. It relies on the efficiency of the matrix method to quantify systematically the effects of rotation and flattening on the eigenmodes of the galaxy. We identify two types of bi-symmetric instabilities for the flatter models – the so-called bending and bar-growing modes – the latter of which persists even for very round models. As anticipated, in its least unstable configurations, the system becomes flatter as its rotational speed increases. More realistic equilibria will be required to achieve a better match to the main sequence of fast-slow rotators. The corresponding code is made public.

Keywords: Diffusion – Gravitation – Galaxies: kinematics and dynamics

1. INTRODUCTION

Rotation is ubiquitous in the universe (Persic et al. 1996; Cappellari et al. 2006; Bianchini et al. 2018). The diversity among galaxies showcases a broad spectrum of mass and angular momentum distributions (Romanowsky & Fall 2012; Teklu et al. 2015). During formation, gravitational forces drive these celestial bodies to collapse, acquiring angular momentum via torques (Barnes & Efstathiou 1987). Thanks to dissipation, the result post virialization is typically a flattened rotating structure (Fall & Efstathiou 1980). Understanding how this geometry and kinematics affects the response of galaxies is important in its own right (e.g., to define stability thresholds, starting with the seminal work of Ostriker & Peebles 1973), but also to explain their long-term evolution through adiabatic or resonant relaxation (Hénon 1964; Binney & Lacey 1988). Such endeavor has been attempted through N -body simulations (e.g. Palmer et al. 1990; Kuijken & Dubinski 1994; Sellwood & Valluri 1997; Breen et al. 2021; Kamlah et al. 2022)¹. A worthy alternative is to follow

the path of Kalnajs (1977); Saha (1991); Weinberg (1994) and compute the linear response of such systems (see, e.g. Petersen et al. 2024, for a recent public distribution of such codes for thin discs and spheres). The knowledge of such response is useful per say (Rozier et al. 2022), but also to quantify their long term evolution: their secular response will be amplified by the square of their corresponding gravitational susceptibility, which can be large when centrifugal support and flattening is important (Weinberg 2001; Fouvy et al. 2015). This is the case for the majority of galaxies across cosmic time (Nair & Abraham 2010).

The impact of rotation and flattening on their linear response is most effectively studied analytically by considering integrable equilibria as a reference point, because it yields trivial unperturbed equations of motions (Kalnajs 1976; de Zeeuw et al. 1986; Robijn & de Zeeuw 1996). Historically, the complexity of moving beyond simple spherical symmetry posed significant challenges (six-dimensional phase space fully coupled via self-gravity), which were first addressed in Robijn (1995) in the so-called thin shell approximation. However, modern computers can now model more complex shapes or kinematics (Rozier et al. 2019), opening the prospects of also extending our understanding beyond the spherical or razor thin geometries. This motivates the present investigation.

Corresponding author: Kerwann Tep
tep@unc.edu

¹ We shall refer to Sellwood & Valluri (1997) as SV97.

This paper studies the linear response of a family of spheroids with varying levels of flattening and rotation, relying on the integrability of oblate Stäckel clusters (de Zeeuw et al. 1986; Dejonghe & de Zeeuw 1988b, hereafter DZ88). It extends Robijn (1995) in that it is not limited to shell orbits and allows for rotation.

Section 2 presents the spheroidal coordinate system and derives angle actions for the Kuzmin–Kutuzov Stäckel family of clusters. Section 3 presents the corresponding linear response theory. We then compute the growing modes of sequences with varying levels of flattening (Section 4) and rotation (Section 5). Section 6 wraps up and discusses prospects.

2. THE OBLATE SPHEROIDAL CLUSTER

Let us review some properties of axisymmetric Stäckel potentials, following de Zeeuw et al. (1986) and DZ88 (section II.a).

2.1. Prolate spheroidal coordinates

We define spheroidal coordinates as the triple (λ, ϕ, ν) , where ϕ is the azimuthal angle from the usual cylindrical coordinates $(R = \sqrt{x^2 + y^2}, \phi, z)$, and where λ, ν are the roots for τ of

$$\frac{R^2}{\tau - a^2} + \frac{z^2}{\tau - c^2} = 1. \quad (1)$$

We shall restrict ourselves to the case $a > c$, meaning that the spheroids of constant λ are prolate, while the hyperboloids of constant ν have two sheets. λ and ν are elliptic coordinates in each meridional plane $\phi = \phi_0$, with foci on the z -axis at $z = \pm\Delta$, which we define as $\Delta = \sqrt{a^2 - c^2}$. We call the coordinates (λ, ν, ϕ) the *confocal elliptic coordinates*, from which we can define other useful parametrizations such as the *elliptic coordinates* (u, v, ϕ) and (ξ, η, ϕ) . We refer to Appendix A.1 and Fig. A1 for more details.

2.2. Angle-action coordinates

The Hamiltonian of the system is given by (see, e.g., equation 3.246 of Binney & Tremaine 2008)

$$H = \frac{p_u^2 + p_v^2}{2\Delta^2(\sinh^2 u + \sin^2 v)} + \frac{p_\phi^2}{2\Delta^2 \sinh^2 u \sin^2 v} + \psi, \quad (2)$$

where ψ is the potential of the system given by Jacobi et al. (1884); de Zeeuw (1985):

$$\psi = \frac{f(\lambda) - f(\nu)}{\lambda - \nu} = \frac{U(u) - V(v)}{\sinh^2 u + \sin^2 v}, \quad (3)$$

and we have the relations

$$U(u) = \frac{f(\lambda)}{\Delta^2}; \quad V(v) = \frac{f(\nu)}{\Delta^2}. \quad (4)$$

The momenta are then given by

$$p_u^2 = 2\Delta^2(E \sinh^2 u - I_3 - U[u]) - \frac{L_z^2}{\sinh^2 u}, \quad (5a)$$

$$p_v^2 = 2\Delta^2(E \sin^2 v + I_3 + V[v]) - \frac{L_z^2}{\sin^2 v}, \quad (5b)$$

where I_3 is a third integral of motion such that $2\Delta^2 I_3 \rightarrow L^2$ as $\Delta \rightarrow 0$ (see, e.g., equation 3.347 of Binney & Tremaine 2008, for an expression). In this formulation, we can express the action coordinates (see, e.g., equation 3.250 of Binney & Tremaine 2008)²

$$J_u = \frac{1}{\pi} \int_{u_0}^{u_1} du p_u, \quad (6a)$$

$$J_v = \frac{1}{\pi} \int_{v_0}^{v_1} dv p_v = \frac{2}{\pi} \int_{\pi/2}^{v_1} dv p_v, \quad (6b)$$

$$J_\phi = L_z. \quad (6c)$$

We refer to appendix C.1 for the exact computation of the boundaries of the “radial” motion, (u_0, u_1) , and of the out-of-plane motion, (v_0, v_1) . Following equation (13) of Binney (2012), the associated angle variables are given by

$$\theta_u = \int_{u_0}^u du' \frac{\partial p_u}{\partial J_u} + \int_{v_0}^v dv' \frac{\partial p_v}{\partial J_u}, \quad (7a)$$

$$\theta_v = \int_{u_0}^u du' \frac{\partial p_u}{\partial J_v} + \int_{v_0}^v dv' \frac{\partial p_v}{\partial J_v}, \quad (7b)$$

$$\theta_\phi = \int_{u_0}^u du' \frac{\partial p_u}{\partial L_z} + \int_{v_0}^v dv' \frac{\partial p_v}{\partial L_z} + \phi. \quad (7c)$$

One can show that, in the spherical limit, the spheroidal coordinates reduce to the spherical coordinates (r, ϑ, ϕ) , such that $\lambda \rightarrow r^2 + a^2$ and $\nu \rightarrow \vartheta$. Furthermore, J_u tends to the radial action J_r while J_v tends to the longitudinal action $J_\vartheta = L - |L_z|$ (see, e.g., de Zeeuw & Hunter 1990).

3. LINEAR RESPONSE THEORY

3.1. The matrix method

Let us consider a self-gravitating stellar cluster, and place ourselves in an inertial frame. We assume that we have access to a complete set of bi-orthogonal basis functions $(\psi^{(p)}[\mathbf{r}], \rho^{(p)}[\mathbf{r}])$ which satisfy

$$\psi^{(p)}(\mathbf{r}) = \int d\mathbf{r}' U(|\mathbf{r} - \mathbf{r}'|) \rho^{(p)}(\mathbf{r}'), \quad (8a)$$

$$\int d\mathbf{r} \psi^{(p)*}(\mathbf{r}) \rho^{(q)}(\mathbf{r}) = -\delta_{pq}, \quad (8b)$$

² We show in appendix A.2 that the action variables (J_u, J_v, L_z) used in the (u, v) formulation are identical to the action variables (J_λ, J_ν, L_z) used in the (λ, ν) formulation.

where we defined the Newtonian interaction potential, $U(r) = -G/r$.

Suppose that the equilibrium is described by a set of angle actions coordinates $(\boldsymbol{\theta}, \mathbf{J})$ given by equations (6)–(7), and a distribution function, $F(\mathbf{J})$ given by equation (27) below. Then, its response matrix, $\mathbf{M}(\omega)$, is defined through its components³

$$M_{pq}(\omega) = (2\pi)^d \sum_{\mathbf{k}} \int d\mathbf{J} \frac{\mathbf{k} \cdot \partial F / \partial \mathbf{J}}{\omega - \mathbf{k} \cdot \boldsymbol{\Omega}(\mathbf{J})} \psi_{\mathbf{k}}^{(p)*} \psi_{\mathbf{k}}^{(q)}, \quad (9)$$

where $\text{Im}(\omega) > 0$, $\boldsymbol{\Omega}(\mathbf{J}) = \partial H_0 / \partial \mathbf{J}$ are the orbital frequencies, d the dimension of physical space and $\psi_{\mathbf{k}}^{(p)}(\mathbf{J})$ is the Fourier transform of the potential basis elements defined by

$$\psi_{\mathbf{k}}^{(p)}(\mathbf{J}) = \int \frac{d\boldsymbol{\theta}}{(2\pi)^d} \psi^{(p)}(\mathbf{r}[\boldsymbol{\theta}, \mathbf{J}]) e^{-i\mathbf{k} \cdot \boldsymbol{\theta}}. \quad (10)$$

We detail this computation in Appendix D.

3.2. Prolate spheroidal basis functions

Let us write the basis elements in a separable way

$$\psi^{\ell mn}(\mathbf{r}) = \frac{\sqrt{4\pi G}}{\Delta} F^{\ell mn}(\xi) Y_{\ell}^m(v, 0) e^{im\phi}. \quad (11)$$

Let $\mathbf{k} = (k_u, k_v, k_\phi)$. Then

$$\psi_{\mathbf{k}}^{\ell mn}(\mathbf{J}) = \frac{\sqrt{4\pi G}}{\Delta} \delta_{k_\phi}^m \frac{1 + (-1)^{\ell+m+k_v}}{2} W_{\mathbf{k}}^{\ell mn}(\mathbf{J}), \quad (12)$$

where

$$W_{\mathbf{k}}^{\ell mn}(\mathbf{J}) = \int_{u_0}^{u_1} \frac{du}{\pi} F^{\ell mn}(\xi) \cos(\alpha_{\mathbf{k}}) \quad (13)$$

$$\times \int_{v_0}^{v_1} \frac{dv}{\pi} |J| Y_{\ell}^m(v, 0) \cos(\beta_{\mathbf{k}}),$$

which is real. In particular, $\psi_{\mathbf{k}}^{\ell mn}(\mathbf{J})$ vanishes for odd values of $\ell + m + k_v$. We detail this computation in Appendix F.

One can check the validity of this expression by computing the potential basis elements via their angular Fourier decomposition

$$F^{\ell mn}(\xi) Y_{\ell}^m(v, \phi) = \sum_{\substack{k_u, k_v \\ \ell+m+k_v \text{ even} \\ k_\phi=m}} W_{k_u k_v}^{\ell mn}(\mathbf{J}) e^{i\mathbf{k} \cdot \boldsymbol{\theta}}. \quad (14)$$

3.3. Linear response of oblate spheroidal clusters

The matrix elements given in equation (9) take the form

$$M_{pq}(\omega) = \delta_{m^q}^{m^p} \frac{32\pi^4 G}{\Delta^2} \sum_{\substack{k_u, k_v \\ \ell^p+m^p+k_v \text{ even} \\ \ell^q+m^q+k_v \text{ even}}} \int d\mathbf{J} \frac{\mathbf{k} \cdot \partial F / \partial \mathbf{J}}{\omega - \mathbf{k} \cdot \boldsymbol{\Omega}} W_{\mathbf{k}}^{(p)} W_{\mathbf{k}}^{(q)}, \quad (15)$$

where $k_\phi = m^p = m^q$. As a consequence, only matrix elements such that ℓ^p and ℓ^q have the same parity are non-zero. To compute the modes of the system, we must solve the equation

$$\det[\mathbf{E}(\omega)] = 0; \quad \mathbf{E}(\omega) = \mathbf{I} - \mathbf{M}(\omega), \quad (16)$$

where $\mathbf{E}(\omega)$ is the dielectric matrix and \mathbf{I} the identity matrix.

The system's axisymmetry, which appears through the Kronecker symbol $\delta_{m^p}^{m^q}$, makes the response matrix a block-diagonal matrix. As such, one can decouple the system's instabilities through their azimuthal number, m , and study separately the axisymmetric modes $m = 0$, the lop-sided modes $m = \pm 1$, the bi-symmetric modes $m = \pm 2$, and so on. Nonetheless, contrary to the infinitely thin disc and the spherically symmetric sphere cases, the axisymmetric response matrix does not benefit from a two-dimensional reduction. As such, one has to face both theoretical and computational difficulties, such as the calculation of orbital frequency, of the angular Fourier transform of the basis elements, and the integration over the full three-dimensional action space.

3.4. Azimuthal response matrix

Owing to axial symmetry, we can decompose the dispersion relation over the azimuthal numbers m as

$$\det \mathbf{E}(\omega) = \prod_m \det \mathbf{E}^m(\omega), \quad (17)$$

with $\mathbf{E}^m(\omega) = \mathbf{I} - \mathbf{M}^m(\omega)$. Here, we define the azimuthal response matrix $\mathbf{M}^m(\omega)$ by

$$M_{pq}^m(\omega) = \frac{32\pi^4 G}{\Delta^2} \sum_{\substack{k_u, k_v \\ \ell^p+m+k_v \text{ even} \\ \ell^q+m+k_v \text{ even}}} \int d\mathbf{J} \frac{\mathbf{k} \cdot \partial F / \partial \mathbf{J}}{\omega - \mathbf{k} \cdot \boldsymbol{\Omega}} W_{\mathbf{k}}^{(p)} W_{\mathbf{k}}^{(q)}, \quad (18)$$

where $\tilde{\mathbf{k}} = (k_u, k_v)$, $k_\phi = m$, $p = (\ell^p, n^p)$ and $q = (\ell^q, n^q)$. Axial symmetry yields the relation

$$M_{pq}^{-m}(\omega)^* = M_{pq}^m(-\omega^*). \quad (19)$$

Therefore, $\omega_0 + i\gamma$ is an m -mode if and only if $-\omega_0 + i\gamma$ is an $(-m)$ -mode, and the analysis can be restricted to $m \geq 0$. In addition, for systems with DF depending only on L_z^2 – e.g., with no rotation – the relation

$$M_{pq}^m(-\omega^*) = M_{pq}^m(\omega)^*, \quad (20)$$

hold, which is obtained by making the change of variables $L_z \mapsto -L_z$. We can thus limit our exploration to the sampling of frequency space over $\text{Re}(\omega) \geq 0$.⁴ In addition, following Rozier et al. (2022), we can show that an accurate

³ If the frame is non-inertial, then we must take into account inertial pseudo-forces in the computation (see, e.g., Rozier et al. 2022).

⁴ These relations only hold *a priori* on the upper frequency plane $\text{Im}(\omega) > 0$, where the integral definition of the response matrix holds. However, they can be extended to the lower part of complex plane after analytic continuation of the response matrix (see, e.g. Weinberg 1994; Fouvry & Prunet 2022, and Appendix I).

computation of the modes $m = -1, 0, 1$ requires the use of inertial pseudo-forces. For the sake of simplicity, we shall restrict our analysis to the bi-symmetric modes $m = 2$.

3.5. Mode shapes

Finally, linear response theory enables us to represent the shape of the unstable modes using the eigenvectors of the response matrix. Specifically, when an unstable mode arises, we obtain an eigenvector, $\mathbf{a} = (a_{\ell n}^m)$, such that

$$\mathbf{M}(\omega) \mathbf{a} = \mathbf{a}. \quad (21)$$

It follows that the shape of the density perturbation, $\delta\rho$, and the potential perturbation, $\delta\psi$, are given by the bi-orthogonal expansions

$$\delta\rho^m(\mathbf{r}) = \sum_{\ell n} a_{\ell n}^m \frac{D^{\ell mn}(\xi)}{c_{\Delta}(\xi, \eta)} Y_{\ell}^m(v, \phi), \quad (22a)$$

$$\delta\psi^m(\mathbf{r}) = \sum_{\ell n} a_{\ell n}^m F^{\ell mn}(\xi) Y_{\ell}^m(v, \phi). \quad (22b)$$

4. APPLICATION: KUZMIN–KUTUZOV MODEL

4.1. Description of the model

The Kuzmin–Kutuzov model is an oblate Stäckel cluster. Indeed, its potential can be expressed in prolate spheroidal coordinates (see Section 2 and Appendix A) using equation (3), with the choice (see, e.g., equation 4.1 of DZ88)

$$f(\tau) = GM(c - \sqrt{\tau}). \quad (23)$$

It follows that its potential reads

$$\psi(\lambda, \nu) = -\frac{GM}{\sqrt{\lambda} + \sqrt{\nu}}, \quad (24)$$

while its associated mass density reads

$$\rho(\lambda, \nu) = \frac{Mc^2}{4\pi} \frac{\lambda\nu + a^2(\lambda + 3\sqrt{\lambda\nu} + \nu)}{(\lambda\nu)^{3/2}(\sqrt{\lambda} + \sqrt{\nu})^3}. \quad (25)$$

Now, let us define the dimensionless quantities (see table 1 of DZ88)

$$\tilde{E} = -\frac{(a+c)E}{GM}; \quad \tilde{L}_z = \frac{L_z}{\sqrt{(a+c)GM}}, \quad (26a)$$

$$\tilde{a} = \frac{a}{a+c}; \quad \tilde{c} = \frac{c}{a+c}. \quad (26b)$$

Defining the squared eccentricity $h = 1 - (c/a)^2$, we can obtain the corresponding two-integral distribution function, $F(E, L_z)$, under the form (DZ88; Batsleer & Dejonghe 1993)

$$F(E, L_z) = f_0 \tilde{E}^{5/2} \sum_{\epsilon=\pm 1} \int_0^1 \frac{dt(1-t^2)}{(1-2\tilde{a}\tilde{E}t\sqrt{1-t^2} + \epsilon\sqrt{z}t)^5} \times [(3+4x_{\epsilon}-x_{\epsilon}^2)(1-x_{\epsilon})(1-t^2)+12t^2], \quad (27)$$

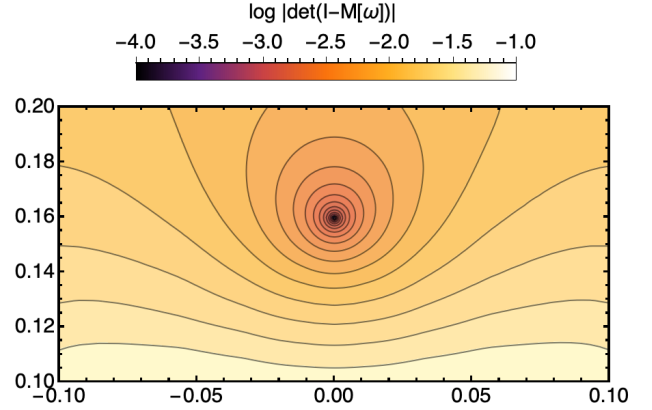


Figure 1. Isocontours of $\det \mathbf{E}(\omega)$ in the upper plane of the frequency space for $m=2$ for the clusters with $a=0.88$. We used the values $\ell_{\max}=30$, $n_{\max}=10$ and $k_{\max}=10$, $256 \times 256 \times 128$ sampling nodes for the (J_u, J_v, L_z) action integrals and 100 sampling nodes for the $W_k^{(p)}$ integrals. Here, we detect a growing mode at $\omega=0.16 i$.

where

$$f_0 = \frac{M}{(GM(a+c))^{3/2}} \frac{\tilde{c}^2}{2^{3/2}\pi^3\tilde{a}}, \quad (28a)$$

$$z = 2h\tilde{E}\tilde{L}_z^2, \quad (28b)$$

$$x_{\epsilon} = 2\tilde{a}\tilde{E}t \frac{\sqrt{1-t^2}}{1 + \epsilon\sqrt{z}t}. \quad (28c)$$

Finally, one can verify that this distribution function reduces to the isotropic isochrone distribution (see, e.g., Hénon 1960; Fouvy et al. 2021) in the spherical limit, and to the fully tangentially anisotropic Toomre distribution function (Miyamoto 1971) in the flat limit (see Appendix E for more details).

In this paper, we shall use the physical units defined by setting $G = M = a + c = 1$.

4.2. Non-rotating bi-symmetric modes

The bi-symmetric instabilities are identified by solving Eq. (16). This is done by computing $\det \mathbf{E}(\omega)$ on a grid in the upper complex frequency plane and searching for its zeros.

This process is illustrated in Fig. 1 for the cluster of flatness $c/a = 0.136$. As increasingly flattened clusters are considered, a greater number of ℓ harmonics are required to achieve convergence toward the physical mode. This arises from the attempt to represent a highly flattened object using spherical harmonics, which are inherently better suited for small perturbations around a spherical shape.

Let us now investigate the impact of flattening on the stability of these clusters by applying this method to a wide range of flattening parameters, c/a . Fig. 2 illustrates both an application of linear theory and its effectiveness in reproducing measurements from simulations. We obtain a 10% agree-

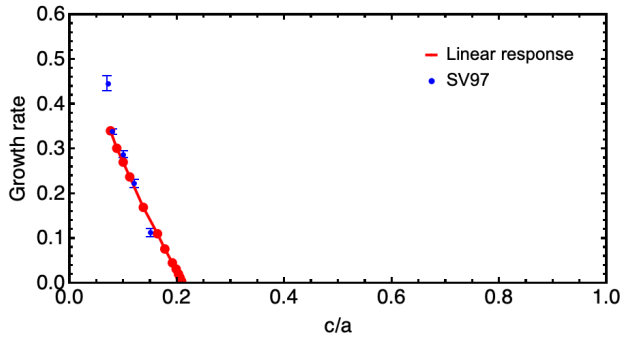


Figure 2. Growth rate as a function of flattening c/a , for the modes $m = 2$ of non-rotating clusters. The predicted growth rate from linear response theory, in red, closely match those measured by SV97, shown in blue.

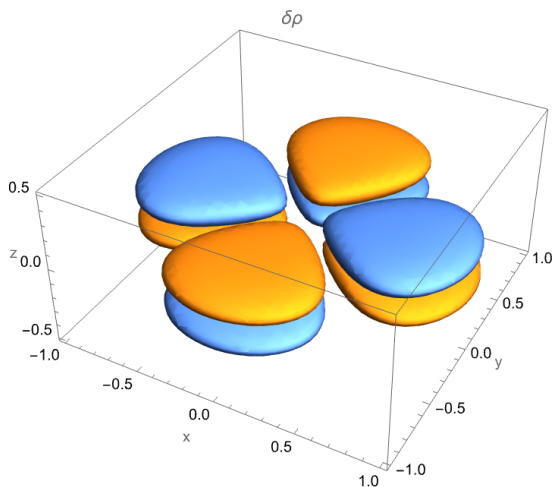


Figure 3. Shape of the $m=2$ density mode of a non-rotating, $a=0.9$ cluster, corresponding to a frequency $\omega \sim 0.22i$. It is saddle-shaped, which corresponds to the shape of bending modes made by SV97.

ment with the measurements of the bending modes made in N -body simulations by SV97. Furthermore, we recover the same transition to stability at the threshold $c/a = 0.208$.

Figure 3 shows the shape of the density perturbation for the $a = 0.9$ cluster, which appears as an saddle-shaped overdensity.

5. INTRODUCING ROTATION

5.1. Response matrix with rotation

Let us introduce rotation to the system by adding an odd component to the distribution function, following Lynden-Bell’s daemon prescription (Lynden-Bell 1960)

$$F_{\text{rot}}(E, L_z) = F(E, L_z)(1 + \alpha_r \text{sgn}[L_z]), \quad (29)$$

where $F_{\text{rot}}(E, L_z)$ is the DF of the rotating cluster, and $F(E, L_z)$ the distribution function of the non-rotating Kuzmin–Kutuzov cluster. This choice is of course somewhat

artificial, but convenient both for theoretical and numerical purposes. Then, the rotational response matrix may be decomposed into two contributions

$$M_{pq}^m(\omega) = M_{pq}^{m,a}[\omega] + \alpha_r (M_{pq}^{m,b}[\omega] + M_{pq}^{m,c}[\omega]), \quad (30)$$

where we specify each component in Appendix G.

5.2. Spin parameter

Let us define the spin parameter (Peebles 1969; Emsellem et al. 2007)

$$\lambda_r = \frac{|L_z^{\text{tot}}| \sqrt{|E^{\text{tot}}|}}{GM}, \quad (31)$$

where the specific mean energy and mean angular momentum are given by

$$E^{\text{tot}} = \frac{(2\pi)^3}{M} \int d\mathbf{J} E(\mathbf{J}) F_{\text{tot}}(\mathbf{J}), \quad (32a)$$

$$L_z^{\text{tot}} = \frac{(2\pi)^3 \alpha_r}{M} \int d\mathbf{J} |L_z| F_{\text{tot}}(\mathbf{J}). \quad (32b)$$

Here, $F_{\text{tot}}(\mathbf{J})$ is the non-rotational Kuzmin–Kutuzov distribution function given by equation (27), while E and L_z are the classical specific integrals of motion. We note that λ_r is proportional to α_r for a given value of c/a , which allows us to easily convert our observation for the Kuzmin cluster into its classical λ_r formulation (Emsellem et al. 2007).

5.3. Rotating bi-symmetric Kuzmin–Kutuzov clusters

In the same spirit as in Section 4.2, let us compare the prediction from linear response theory to measurements made in N -simulations by SV97. The impact of flattening on growth rate for a rapidly rotating cluster $\alpha_r = 0.75$ and the maximally rotating cluster $\alpha_r = 1$ is shown in Fig. 4. First, we note an agreement with N -body measurements within 10% accuracy, as well as matching behavior w.r.t. flattening ratio. In addition, we observe a steep increase of the growth rate as one considers very flattened clusters. Conversely, flattened systems tend to become more and more stable as they become rounder for any rotation parameters. In particular, the cluster with rotation parameter $\alpha_r = 0.75$ become completely stable at $c/a \sim 0.6$, while the maximally rotating clusters become stable at $c/a = 1$.⁵ While SV97 appear not to measure any such instabilities beyond $c/a = 0.6$, this may be explained either by the low growth rate prediction by linear theory ($\gamma < 0.07$), and/or by the impact of softening on the growth rate (De Rijcke et al. 2019; Roule 2024). Finally, linear theory provides us with a tool to systematically perform the stability analysis w.r.t. to the flattening ratio of the

⁵ This is reminiscent of conclusions made by Rozier et al. (2019), who showed that the similar isotropic Plummer cluster was stable for any rotation parameter.

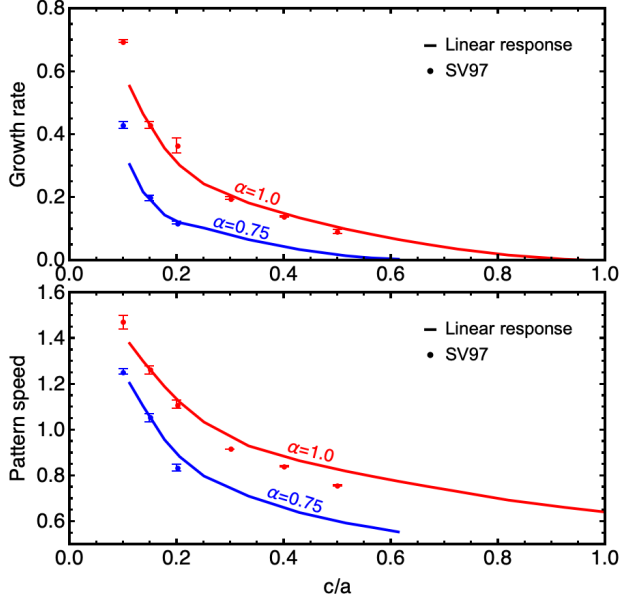


Figure 4. Growth rate (top panel) and pattern speed (bottom panel) as a function of flattening c/a , for the modes $m = 2$ of fast rotating clusters $\alpha_r = 0.75$ (in blue) and maximally rotating clusters $\alpha_r = 1$ (in red). Full lines are the predicted growth rate from linear response theory, while dots are those measured by SV97. The stability of the Kuzmin–Kutuzov cluster increases as it approaches the spherical limit, with the maximally rotating configuration being the last to achieve stability at $c/a = 1$.

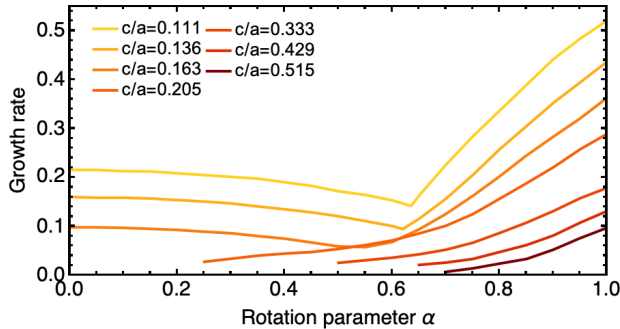


Figure 5. The growth rate of the dominant $m = 2$ mode is shown as a function of rotation for clusters with a fixed flattening ratio c/a . A clear transition is observed from bending modes to bar-growing modes in highly flattened clusters, with the growth rate reaching a minimum at the point of transition. This is illustrated in Fig. K1 of Appendix K, which displays the behavior of each modes in their subdominant regimes.

cluster, c/a , and its rotation parameter, α_r , which we convert into the associated spin parameter, λ_r .

We represent this overall analysis in Figs. 5 and 6. We identify four regions of interest. First, we recover the dependence of the stability of non-rotating clusters on their flattening by examining the $\lambda_r = 0$ axis, where the stability threshold occurs at $c/a = 0.208$. Secondly, in highly flattened systems with relatively low spin parameters, the growth rate

decreases as rotation increases. These are the bending modes measured by SV97, and are illustrated in the left panel of Fig. 7. However, beyond a given rotation threshold, which depends on the cluster’s flattening, the dominant mode is a so-called bar-growing mode, whose shape presents a distinctive bi-symmetric spiral structure (see right panel of Fig. 7). Moreover, these modes seem to persist across a much broader range of flattening ratios, with the maximally rotating clusters being the last to stabilize as the system approaches the spherical limit. Finally, there appears to be a region of stability in the parameter space for cluster which are not too flattened and have a low enough rotation parameter.

5.4. Transition to damped bar modes

We may perform analytic continuation on the matrix elements in order to study the transition to stability of the bar-growing modes. We refer to Appendix I for further details. Figure 8 shows the growth rate of a $c/a = 0.613$ cluster w.r.t. the rotation parameter, α_r . The cluster becomes stable at a non-zero rotation parameter, before exhibiting damped modes below that threshold.

However, such stability analysis cannot be performed for an arbitrary cluster. Indeed, the calculation of the response matrix close to the real frequency axis may become a numerical challenge due the resonant denominator – especially for low values of $\text{Re}(\omega)$. Therefore, when studying the marginal stability of non-rotating clusters around $c/a = 0.208$, careful attention must be given to the integration in action space. While a change of variables similar to that used by Fouvry & Prunet (2022) might be of interest, such a transformation has yet to be developed within the context of axisymmetric systems.

6. CONCLUSIONS AND PERSPECTIVES

Nearly 30 years after the seminal work of Robijn (1995), this paper extended linear response theory to rotating oblate Stäckel clusters. Our implementation was validated against the results from SV97, showing that the converged $m = 2$ modes of flattened and rotating spheroids closely match N -body simulations at the $\sim 10\%$ level in terms of growth rates (see Figs. 2 and 4), pattern speeds, and shapes. When rotation is introduced, two families of fast and slow modes are found (Figs. 3 and 7): the bending modes, which are saddle-shaped, and the bar-growing modes, which are spiral shaped. Our implementation also allows for analytic continuation so that certain weakly damped modes can be identified (see Fig. 8). However, a more systematic study (for, e.g., the marginal stability of non-rotating clusters) would require a more careful treatment of the resonant denominator of the response matrix, which becomes sharp near the real frequency line.

Note that breaking spherical symmetry introduces various theoretical and computational challenges when applying lin-

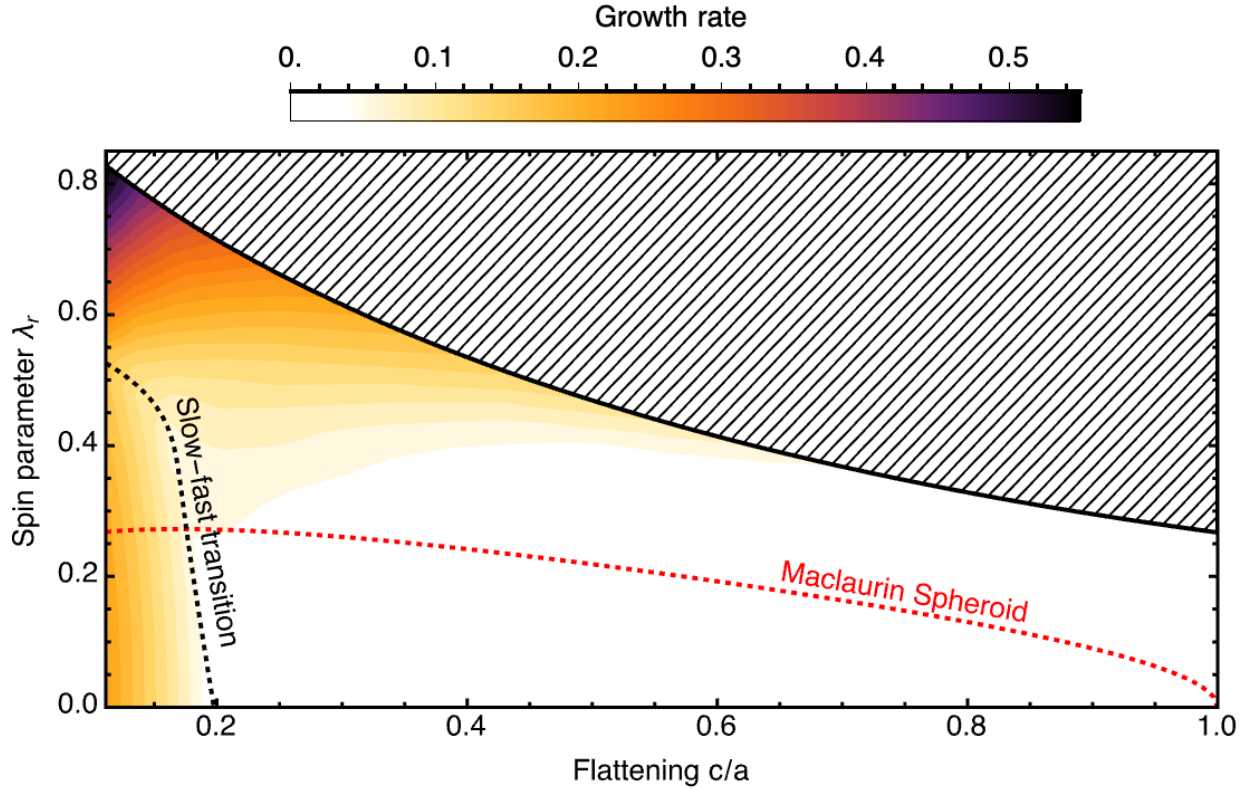


Figure 6. Dependency of the $m = 2$ growth rates w.r.t. flattening c/a and spin parameter, λ_r . The hashed region corresponds to the parameters which cannot be attained by a single-component Stäckel cluster. For highly flattened clusters, a transition (dashed black line) between slowly rotating bending modes (Fig. 7, left panel) and rapidly rotating bar-growing modes (Fig. 7, right panel) occurs. For models rounder than $c/a = 0.2$, the clusters are either stable or subject to the latter instability. We refer to Fig. 5 for a sample of c/a -slices of the growth rate. Finally, we show in dashed red the behavior of the stable Maclaurin spheroids for comparison purpose, which display a much different behavior than the Kuzmin–Kutuzov clusters.

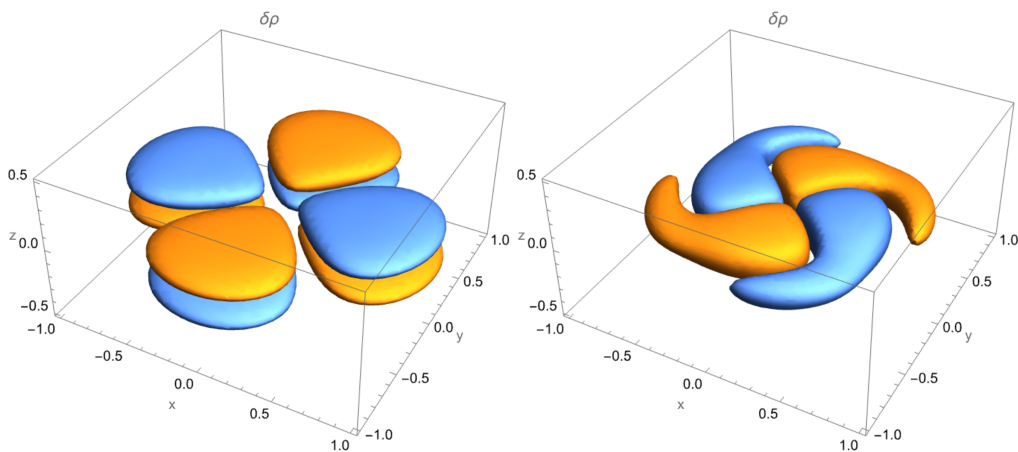


Figure 7. Shape of the $m = 2$ density modes of a $a = 0.9$ cluster, for the two types of rotating instabilities. *Left panel:* slow bending mode ($\alpha_r = 0.4$, $\omega = 0.12 + 0.19i$). *Right panel:* Fast bar-growing mode ($\alpha_r = 1.0$, $\omega = 1.31 + 0.53i$). We highlight the impact of rotation in Fig. H1 of appendix H. The fast rotating mode, however, corresponds to a distinct family of instability, with a much higher pattern speed, and strikingly, presents a very different shape.

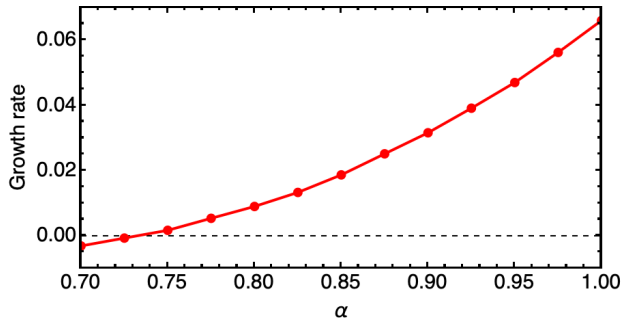


Figure 8. Evolution of the growth rate of a $c/a = 0.613$ cluster w.r.t. the rotation parameter α_r . Transition from damped bar modes (on the left) to unstable bar modes occurs at a fixed value as we increases α_r .

ear response theory. While axial symmetry allowed us to decompose the response matrix into distinct azimuthal components, it also fundamentally transformed the computational problem into a three-dimensional one. Specifically, computing a 5×5 frequency-space grid for the response matrix of a single cluster with $(\ell_{\max}, n_{\max}, k_{\max}) = (30, 10, 10)$, and performing the action-space integration over $256 \times 256 \times 128$ nodes, required approximately 38 hours across 512 CPU cores. Hence we had to carefully balance mode convergence with computational cost to achieve accurate predictions. On the other hand, this formalism provides access to the system’s linear response across all values of α_r , as per equation (30). Consequently, future studies may find it advantageous to revisit this type of analysis with improved computational resources.

Although this single-component asymptotically cold model is not realistic enough to compare against data (e.g. Emsellem et al. 2007, and subsequent work) and simulations (e.g. Choi et al. 2018), the formalism presented here may easily be extended to multi-component Stäckel systems, and therefore eventually be applied to more realistic equilibria.

6.1. Perspectives

One should first investigate the limitations of the specificities of this Stäckel model, which extends the one-component, isotropic isochrone sphere to flattened systems. Further exploration would be beneficial to extend the computation of linear response to more realistic spheroids, incorporating three-integral distribution functions (see, e.g., section IV.d of Dejonghe & de Zeeuw 1988b), two- or three-component Stäckel discs and halos (Dejonghe & de Zeeuw 1988a; Hunter & Qian 1993; Batsleer & Dejonghe 1994; Famaey & Dejonghe 2003; Petač & Ullio 2019; Gromov & Nikiforov 2021; Koppelman & Helmi 2021), or empirically fitted distributions (Dejonghe 1989; Famaey et al. 2002). It would also be interesting to examine the linear stability of elliptical clusters (Wilkinson & James 1982; de Zeeuw & Franx 1991; Merritt 1999; Padilla & Strauss 2008) or to investigate

more sophisticated models of rotation, though computational complexity might quickly become a heavily limiting factor. Furthermore, the transposition the present formalism into the time domain following, e.g., Rozier et al. (2022) (and references therein), remains an open problem, as is the inclusion of pseudo-forces in the calculation of axisymmetric and lopsided instabilities.

Beyond linear response, the methodology could be naturally expanded to kinetic theory (Roule et al. 2022; Roule 2024), say, to address the secular vertical heating of thick discs while improving upon perturbative studies (Fouvry et al. 2017). Such investigations could offer deeper insights into the evolutionary trajectories of galactic systems, enabling comparisons across galaxy populations over cosmic timescales and within diverse environments (Gardner et al. 2006; Castellano et al. 2022; Naidu et al. 2022).

Eventually, understanding statistically (beyond the mean response, see Touchette 2009; Feliachi & Fouvry 2023) the impact of rotation and flattening should prove critical to model the morphological evolution of populations of galaxies across cosmic times (see, e.g., Lintott et al. 2008; Conselice 2014). Indeed, the distribution of angular momentum is, beyond mass, the most relevant dynamical parameter for such populations: it separates elliptical galaxies from spiral ones (Hernandez & Cervantes-Sodi 2006). The long-term impact of rotation on galactic orbital structures will therefore be the focus of our future research.

DATA DISTRIBUTION

The data underlying this article is available through reasonable request to the author. The notebook used to compute the bi-orthogonal basis function is distributed at the URL: <https://github.com/KerwannTEP/SPOCK>. The code used for the computation of the linear response, written in Julia (Bezanson et al. 2017), is also now part of the general purpose Julia stellar dynamics codes found at <https://github.com/JuliaStellarDynamics>, as discussed by Petersen et al. (2024).

ACKNOWLEDGEMENTS

We are grateful to J.-B. Fouvry, M. Roule, M. Weinberg and A. L. Varri for numerous suggestions during the completion of this work, which is partially supported by the grant *SEGAL* ANR-19-CE31-0017 of the French Agence Nationale de la Recherche and by the National Science Foundation under Grants No. AST-2310362 to the University of North Carolina and No. PHY-2309135 to the Kavli Institute for Theoretical Physics (KITP). We thank Stéphane Roubertol for the smooth running of the Infinity cluster, where part of the computations was performed. We would like to also thank the University of North Carolina at Chapel Hill and the Research Computing group for providing computational re-

sources and support that have contributed to these research results.

REFERENCES

- Abramowitz M., Stegun I. A., eds, 1972, *Handbook of Mathematical Functions with Formulas, Graphs, and Mathematical Tables*, tenth printing edn. U.S. Government Printing Office, Washington, DC, USA
- Bar-Or B., Alexander T., 2016, *ApJ*, **820**, 129
- Barnes J., Efstathiou G., 1987, *ApJ*, **319**, 575
- Batsleer P., Dejonghe H., 1993, *AAP*, **271**, 104
- Batsleer P., Dejonghe H., 1994, *A&A*, **287**, 43
- Bezanson J., Edelman A., Karpinski S., Shah V. B., 2017, *SIAM Review*, **59**, 65
- Bianchini P., van der Marel R. P., del Pino A., Watkins L. L., Bellini A., Fardal M. A., Libralato M., Sills A., 2018, *MNRAS*, **481**, 2125
- Binney J., 2012, *MNRAS*, **426**, 1324
- Binney J., Lacey C., 1988, *MNRAS*, **230**, 597
- Binney J., Tremaine S., 2008, *Galactic Dynamics: Second Edition*
- Breen P. G., Rozier S., Heggie D. C., Varri A. L., 2021, *MNRAS*, **502**, 4762
- Cappellari M., et al., 2006, *MNRAS*, **366**, 1126
- Castellano M., et al., 2022, *ApJL*, **938**, L15
- Chandrasekhar S., 1969, *Ellipsoidal figures of equilibrium*
- Choi H., Yi S. K., Dubois Y., Kimm T., Devriendt J. E. G., Pichon C., 2018, *ApJ*, **856**, 114
- Conselice C. J., 2014, *ARA&A*, **52**, 291
- De Rijcke S., Fouvy J.-B., Dehnen W., 2019, *MNRAS*, **485**, 150
- Dejonghe H., 1989, *ApJ*, **343**, 113
- Dejonghe H., de Zeeuw T., 1988a, *ApJ*, **329**, 720
- Dejonghe H., de Zeeuw T., 1988b, *ApJ*, **333**, 90
- Emsellem E., et al., 2007, *MNRAS*, **379**, 401
- Eyre A., 2010, *arXiv e-prints*, p. [arXiv:1010.3382](https://arxiv.org/abs/1010.3382)
- Fall S. M., Efstathiou G., 1980, *MNRAS*, **193**, 189
- Famaey B., Dejonghe H., 2003, *MNRAS*, **340**, 752
- Famaey B., Van Caelenberg K., Dejonghe H., 2002, *MNRAS*, **335**, 201
- Feliachi O., Fouvy J.-B., 2023, *arXiv*, [2308.08308](https://arxiv.org/abs/2308.08308)
- Fouvy J.-B., Prunet S., 2022, *MNRAS*, **509**, 2443
- Fouvy J. B., Pichon C., Magorrian J., Chavanis P. H., 2015, *A&A*, **584**, A129
- Fouvy J.-B., Pichon C., Chavanis P.-H., Monk L., 2017, *MNRAS*, **471**, 2642
- Fouvy J.-B., Hamilton C., Rozier S., Pichon C., 2021, *MNRAS*, **508**, 2210
- Gardner J. P., et al., 2006, *SSRv*, **123**, 485
- Gromov A. O., Nikiforov I. I., 2021, *Astrophysical Bulletin*, **76**, 146
- Hénon M., 1960, *Annales d’Astrophysique*, **23**, 474
- Hénon M., 1964, *Annales d’Astrophysique*, **27**, 83
- Hénon M. H., 1971, *Ap&SS*, **14**, 151
- Hernandez X., Cervantes-Sodi B., 2006, *Monthly Notices of the Royal Astronomical Society*, **368**, 351
- Hunter C., Qian E., 1993, *MNRAS*, **262**, 401
- Jacobi C., Lottner E., Borchardt C. W., Clebsch A., 1884, *Vorlesungen über Dynamik*. Berlin, G. Reimer, 1884
- Kalnajs A. J., 1976, *ApJ*, **205**, 751
- Kalnajs A. J., 1977, *ApJ*, **212**, 637
- Kamlah A. W. H., et al., 2022, *Monthly Notices of the Royal Astronomical Society*, **516**, 3266
- Koppelman H. H., Helmi A., 2021, *A&A*, **649**, A55
- Kuijken K., Dubinski J., 1994, *MNRAS*, **269**, 13
- Lintott C. J., et al., 2008, *Monthly Notices of the Royal Astronomical Society*, **389**, 1179
- Lynden-Bell D., 1960, *MNRAS*, **120**, 204
- Merritt D., 1999, *PASP*, **111**, 129
- Miyamoto M., 1971, *PASJ*, **23**, 21
- Naidu R. P., et al., 2022, *ApJL*, **940**, L14
- Nair P. B., Abraham R. G., 2010, *The Astrophysical Journal Supplement Series*, **186**, 427
- Ostriker J. P., Peebles P. J. E., 1973, *ApJ*, **186**, 467
- Padilla N. D., Strauss M. A., 2008, *MNRAS*, **388**, 1321
- Palmer P. L., Papaloizou J., Allen A. J., 1990, *MNRAS*, **243**, 282
- Peebles P. J. E., 1969, *ApJ*, **155**, 393
- Persic M., Salucci P., Stel F., 1996, *MNRAS*, **281**, 27
- Petač M., Ullio P., 2019, *PhRvD*, **99**, 043003
- Petersen M. S., Roule M., Fouvy J.-B., Pichon C., Tep K., 2024, *MNRAS*,
- Robijn F. H. A., 1995, PhD thesis, Leiden Observatory
- Robijn F. H. A., Earn D. J. D., 1996, *MNRAS*, **282**, 1129
- Robijn F. H. A., de Zeeuw P. T., 1996, *MNRAS*, **279**, 673
- Romanowsky A. J., Fall S. M., 2012, *ApJS*, **203**, 17
- Roule M., 2024, PhD thesis
- Roule M., Fouvy J.-B., Pichon C., Chavanis P.-H., 2022, *PhRvE*, **106**, 044118
- Rozier S., Fouvy J. B., Breen P. G., Varri A. L., Pichon C., Heggie D. C., 2019, *MNRAS*, **487**, 711
- Rozier S., Famaey B., Siebert A., Monari G., Pichon C., Ibata R., 2022, *ApJ*, **933**, 113
- Saha P., 1991, *MNRAS*, **248**, 494
- Sellwood J. A., Valluri M., 1997, *MNRAS*, **287**, 124
- Stoer J., Bulirsch R., 1980, *Introduction to Numerical Analysis*. Springer

- Teklu A. F., Remus R.-S., Dolag K., Beck A. M., Burkert A.,
Schmidt A. S., Schulze F., Steinborn L. K., 2015, *ApJ*, 812, 29
- Tep K., Fouvy J.-B., Pichon C., 2022, *MNRAS*, 514, 875
- Toomre A., 1963, *ApJ*, 138, 385
- Touchette H., 2009, *PhR*, 478, 1
- Weinberg M. D., 1994, *ApJ*, 421, 481
- Weinberg M. D., 2001, *MNRAS*, 328, 321
- Wilkinson A., James R. A., 1982, *MNRAS*, 199, 171
- de Zeeuw T., 1985, *MNRAS*, 216, 599
- de Zeeuw T., Franx M., 1991, *ARA&A*, 29, 239
- de Zeeuw P. T., Hunter C., 1990, *ApJ*, 356, 365
- de Zeeuw T., Peletier R., Franx M., 1986, *MNRAS*, 221, 1001

APPENDIX

A. PROLATE SPHEROIDAL COORDINATES

A.1. Definition and conventions

We defined in Section 2.1 the *confocal elliptic coordinates* (λ, ν, ϕ) , which straightforwardly relate to cylindrical coordinates as

$$R^2 = \frac{(\lambda - a^2)(\nu - a^2)}{c^2 - a^2}; \quad z^2 = \frac{(\lambda - c^2)(\nu - c^2)}{a^2 - c^2}. \quad (\text{A1})$$

We illustrate this coordinate system in Fig. A1. While this formulation is widely used in old literature, more recent papers tend to use the *elliptic coordinates* (u, v) (see, e.g., Binney 2012), which parametrize the *confocal elliptic coordinates* as

$$\lambda = a^2 \cosh^2 u - c^2 \sinh^2 u = c^2 + \Delta^2 \cosh^2 u, \quad (\text{A2a})$$

$$\nu = c^2 \sin^2 v + a^2 \cos^2 v = c^2 + \Delta^2 \cos^2 v. \quad (\text{A2b})$$

In particular, it follows that

$$R = \Delta \sqrt{(\xi^2 - 1)(1 - \eta^2)}; \quad z = \Delta \xi \eta, \quad (\text{A3})$$

where we define the coordinates (ξ, η) by setting

$$\xi = \cosh u; \quad \eta = \cos v, \quad (\text{A4})$$

as they are useful when using potential-density basis elements (Robijn & Earn 1996). Finally, the reverse transformation $(R, z) \mapsto (\xi, \eta)$ is given by

$$\xi = \frac{1}{2\Delta} (\sqrt{R^2 + (z + \Delta)^2} + \sqrt{R^2 + (z - \Delta)^2}), \quad (\text{A5a})$$

$$\eta = \frac{1}{2\Delta} (\sqrt{R^2 + (z + \Delta)^2} - \sqrt{R^2 + (z - \Delta)^2}). \quad (\text{A5b})$$

A.2. Relations between (u, v, ϕ) and (λ, ν, ϕ) coordinates

If we denote by I_3 the third integral in (u, v, ϕ) coordinates and by \tilde{I}_3 that in (λ, ν, ϕ) (see, e.g., DZ88), then we have the relation

$$\tilde{I}_3 = \frac{1}{2} (2\Delta^2 E + 2\Delta^2 I_3 - L_z^2), \quad (\text{A6})$$

for any axisymmetric Stäckel potential, which we can obtain by evaluating p_u and p_λ at their boundaries of motions, coupled with equations (A2). In particular, letting $I_2 = L_z^2/2$, we obtain the spherical limit

$$I_2 + \tilde{I}_3 \rightarrow \frac{L^2}{2}. \quad (\text{A7})$$

A large fraction of distribution functions referenced in the literature (DZ88; Robijn & de Zeeuw 1996; Famaey et al. 2002; Famaey & Dejonghe 2003) involving a third integral,

should be understood as functions of (E, I_2, \tilde{I}_3) . They can be converted to functions of (E, I_2, I_3) by using the above equation.

Now, we can show from this relation that

$$p_\lambda^2 = 4\Delta^2 \cosh^2 u \sinh^2 u p_u^2, \quad (\text{A8})$$

where p_λ is the conjugate momentum to λ defined by (DZ88)

$$p_\lambda^2 = \frac{1}{2(\lambda - a^2)} \left(E - \frac{I_2}{\lambda - a^2} - \frac{\tilde{I}_3}{\lambda - c^2} - \frac{f[\lambda]}{\lambda - c^2} \right). \quad (\text{A9})$$

Therefore, for a given orbit, the action variables associated to u and λ are equal, i.e.

$$J_\lambda = \frac{1}{\pi} \int_{\lambda_0}^{\lambda_1} d\lambda p_\lambda = \frac{1}{\pi} \int_{u_0}^{u_1} du p_u = J_u. \quad (\text{A10})$$

Similarly, one can show that

$$p_\nu^2 = 4\Delta^2 \cos^2 v \sin^2 v p_v^2, \quad (\text{A11})$$

where p_ν is the conjugate momentum to ν defined by (DZ88)

$$p_\nu^2 = \frac{1}{2(\nu - a^2)} \left(E - \frac{I_2}{\nu - a^2} - \frac{\tilde{I}_3}{\nu - c^2} - \frac{f[\nu]}{\nu - c^2} \right), \quad (\text{A12})$$

and therefore

$$J_\nu = \frac{2}{\pi} \int_{c^2}^{\nu_1} d\nu p_\nu = \frac{2}{\pi} \int_{\frac{\pi}{2}}^{v_1} dv p_v = J_v. \quad (\text{A13})$$

B. CHANGES OF COORDINATES

The transformation $(E, I_3, L_z) \mapsto (J_u, J_v, L_z)$ is carried out by a straight computation of the two action integrals. However, the inverse transformation lacks an explicit analytical expression. Nevertheless, it can be computed using Newton's method.

Let us define the vectors $\mathbf{J} = (J_u, J_v, L_z)^T$ and $\mathbf{w} = (E, I_3, L_z)^T$. Let us also define the function $\mathbf{j}(\mathbf{w}) = (J_u[\mathbf{w}], J_v[\mathbf{w}], L_z)^T - \mathbf{J}$. We wish to solve $\mathbf{j}(\mathbf{w}) = 0$. We start from an initial guess $\mathbf{w}_0 = (E_i, I_{3,i}, L_z)$ with $I_{3,i} = L_z^2/(2\Delta^2) - E_0$ and $E_i = E_s(L_z, I_{3,i})/2$, which always describes a bound orbit for a Kuzmin–Kutuzov potential. Then, we define for each step

$$\mathbf{w}_{n+1} = \mathbf{w}_n - [J(\mathbf{w}_n)]^{-1} \mathbf{j}(\mathbf{w}_n), \quad (\text{B14})$$

where $J(\mathbf{w})$ is the Jacobian given by

$$J(\mathbf{w}) = \begin{pmatrix} \frac{\partial J_u}{\partial E} & \frac{\partial J_u}{\partial I_3} & \frac{\partial J_u}{\partial L_z} \\ \frac{\partial J_v}{\partial E} & \frac{\partial J_v}{\partial I_3} & \frac{\partial J_v}{\partial L_z} \\ 0 & 0 & 1 \end{pmatrix}. \quad (\text{B15})$$

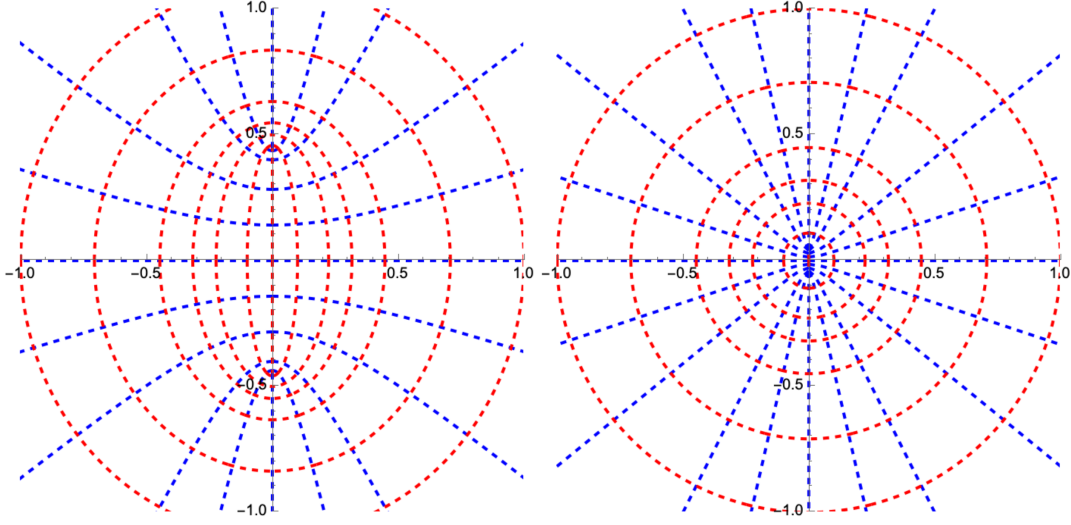


Figure A1. Two-dimensional cut of the spheroidal coordinate system, viewed sideway to the equatorial plane. Blue dashed lines are contours of constant η , while red dashed lines are contours of constant ξ . On the left panel, $a = 0.6$ and $c = 0.4$. The two focal points are located at $z = \pm\Delta$, with $\Delta = 0.447$ in this figure. On the right panel, $a = 0.501$ and $c = 0.499$. The spheroidal coordinates converge to the spherical coordinates in the spherical limit.

At each step, we should be careful not to go outside of the authorized region of (E, L_z, I_3) .

C. STÄCKEL POTENTIAL

C.1. Boundaries of motion

We may define the effective potentials

$$U_{\text{eff}}(u, I_3, L_z) = \frac{L_z^2}{2\Delta^2 \sinh^4 u} + \frac{U(u) + I_3}{\sinh^2 u}, \quad (\text{C16a})$$

$$V_{\text{eff}}(v, I_3, L_z) = \frac{L_z^2}{2\Delta^2 \sin^4 v} - \frac{V(v) + I_3}{\sin^2 v}, \quad (\text{C16b})$$

such that

$$p_u^2 = 2\Delta^2 \sinh^2 u (E - U_{\text{eff}}[u, I_3, L_z]), \quad (\text{C17a})$$

$$p_v^2 = 2\Delta^2 \sin^2 v (E - V_{\text{eff}}[v, I_3, L_z]). \quad (\text{C17b})$$

The boundaries of motions are then computed by solving the equations $p_u^2[u, I_3, L_z] = 0$ and $p_v^2[v, I_3, L_z] = 0$ using bisection.

For given (I_3, L_z) , the shell orbits, i.e., the orbits of constant coordinates u , are given by finding the minimum of $U_{\text{eff}}[u, I_3, L_z]$ w.r.t. u .

C.2. Orbital frequencies and action derivatives

Let us compute the orbital frequencies $\Omega = (\Omega_u, \Omega_v, \Omega_\phi)$. Following Binney (2012), the matrix

$$\begin{pmatrix} \Omega_u & \Omega_v & \Omega_\phi \\ \frac{\partial I_3}{\partial J_u} & \frac{\partial I_3}{\partial J_v} & \frac{\partial I_3}{\partial L_z} \\ 0 & 0 & 1 \end{pmatrix}, \quad (\text{C18})$$

where $\Omega_t = \partial E / \partial J_t$ with $t = u, v, \phi$, is the inverse of the matrix

$$\begin{pmatrix} \frac{\partial J_u}{\partial E} & \frac{\partial J_u}{\partial I_3} & \frac{\partial J_u}{\partial L_z} \\ \frac{\partial J_v}{\partial E} & \frac{\partial J_v}{\partial I_3} & \frac{\partial J_v}{\partial L_z} \\ 0 & 0 & 1 \end{pmatrix}. \quad (\text{C19})$$

To compute the derivative in this second matrix, we need the derivatives of p_u and p_v with respect to E, I_3 and L_z

$$\frac{\partial p_u}{\partial E} = \frac{\Delta^2 \sinh^2 u}{p_u}, \quad \frac{\partial p_v}{\partial E} = \frac{\Delta^2 \sin^2 v}{p_v}, \quad (\text{C20a})$$

$$\frac{\partial p_u}{\partial I_3} = -\frac{\Delta^2}{p_u}, \quad \frac{\partial p_v}{\partial I_3} = \frac{\Delta^2}{p_v}, \quad (\text{C20b})$$

$$\frac{\partial p_u}{\partial L_z} = -\frac{L_z}{p_u \sinh^2 u}, \quad \frac{\partial p_v}{\partial L_z} = -\frac{L_z}{p_v \sin^2 v}, \quad (\text{C20c})$$

C.3. Effective anomaly

Finding an explicit effective anomaly like in the Keplerian case (Bar-Or & Alexander 2016), the isochrone case (Fouvy et al. 2021) or the Plummer case (Tep et al. 2022) is a very difficult process, and requires a case-by-case exploration. In general, an explicit analytical effective anomaly does not exist, and we must content with a numerical evaluation (Hénon 1971; Roule et al. 2022; Petersen et al. 2024). Let $t = u, v$. Following Eyre (2010), we define $\bar{t} = (t_0 + t_1)/2$ and $\hat{t} = (t_1 - t_0)/2$. We let

$$t = \hat{t} \sin \theta + \bar{t}, \quad (\text{C21})$$

for $-\pi/2 \leq \theta \leq \pi/2$. In particular,

$$(t - t_0)(t_1 - t) = \tilde{t}^2 \cos^2 \theta. \quad (\text{C22})$$

Now, in order to compute frequencies and inverse coordinate transformations, we wish to compute integrals of the form

$$I = \int_{t_0}^{t_1} dt \frac{g(t)}{p_t(t)}, \quad (\text{C23})$$

for some well defined function $g(t)$. We know that the momentum behaves as

$$p_t(t) = A\sqrt{|t - t_x|} + \frac{B}{\sqrt{|t - t_x|}} + \dots, \quad (\text{C24})$$

when $t \rightarrow t_x$, for $t_x = t_0, t_1$ and some constants A and B . Therefore, we may write

$$p_t(t) = \sqrt{(t - t_0)(t_1 - t)} \tilde{p}_t(t). \quad (\text{C25})$$

This makes $1/\tilde{p}_t(t)$ a theoretically perfectly well-defined function. It follows from a change of variable $t \mapsto \theta$ that

$$I = \int_{-\pi/2}^{\pi/2} d\theta \frac{g(t[\theta])}{\hat{p}_t(t[\theta])}, \quad \hat{p}_t(t[\theta]) = \frac{p_t(t[\theta])}{\tilde{t} \cos \theta}, \quad (\text{C26})$$

making the integrand non-singular. We can then evaluate it using usual standard quadrature techniques. The limit at the boundaries of motion $t = t_0, t_1$ are given by

$$\tilde{p}_t(t) \rightarrow \frac{1}{\sqrt{t_1 - t_0}} \sqrt{\left| \frac{\partial(p_t^2)}{\partial t} \right|_{t=t_0, t_1}}. \quad (\text{C27})$$

C.4. Action derivatives of the momenta

In order to compute the angles, we need to compute the action derivatives of p_u and p_v , which are to be understood as functions of (J_u, J_v, L_z) . We get

$$\frac{\partial p_t}{\partial J_u} = \frac{\partial p_t}{\partial E} \frac{\partial E}{\partial J_u} + \frac{\partial p_t}{\partial L_z} \frac{\partial L_z}{\partial J_u} + \frac{\partial p_t}{\partial I_3} \frac{\partial I_3}{\partial J_u}, \quad (\text{C28a})$$

$$\frac{\partial p_t}{\partial J_v} = \frac{\partial p_t}{\partial E} \frac{\partial E}{\partial J_v} + \frac{\partial p_t}{\partial L_z} \frac{\partial L_z}{\partial J_v} + \frac{\partial p_t}{\partial I_3} \frac{\partial I_3}{\partial J_v}, \quad (\text{C28b})$$

$$\frac{\partial p_t}{\partial L_z} = \frac{\partial p_t}{\partial E} \frac{\partial E}{\partial L_z} + \frac{\partial p_t}{\partial L_z} \frac{\partial L_z}{\partial L_z} + \frac{\partial p_t}{\partial I_3} \frac{\partial I_3}{\partial L_z}, \quad (\text{C28c})$$

where $t = u, v$ and the momenta of the right hand-side are functions of (E, L_z, I_3) . We may rewrite this system of equations in the matrix form

$$\begin{pmatrix} \frac{\partial p_t}{\partial J_u} \\ \frac{\partial p_t}{\partial J_v} \\ \frac{\partial p_t}{\partial L_z} \end{pmatrix} = \begin{pmatrix} \Omega_u & \Omega_v & \Omega_\phi \\ \frac{\partial I_3}{\partial J_u} & \frac{\partial I_3}{\partial J_v} & \frac{\partial I_3}{\partial L_z} \\ 0 & 0 & 1 \end{pmatrix}^T \begin{pmatrix} \frac{\partial p_t}{\partial E} \\ \frac{\partial p_t}{\partial I_3} \\ \frac{\partial p_t}{\partial L_z} \end{pmatrix}. \quad (\text{C29})$$

D. PROLATE SPHEROIDAL BASIS ELEMENTS

The Robijn basis elements for prolate spheroidal coordinates (ξ, η, ϕ) take the form (see section 3.2 of [Robijn & Earn 1996](#))

$$\psi^{\ell mn}(\mathbf{r}) = \frac{\sqrt{4\pi G}}{\Delta} F^{\ell mn}(\xi) \Phi^{\ell m}(\eta) e^{im\phi}, \quad (\text{D30a})$$

$$\rho^{\ell mn}(\mathbf{r}) = \frac{1}{\sqrt{4\pi G \Delta}} \frac{D^{\ell mn}(\xi)}{c_\Delta(\xi, \eta)} \Phi^{\ell m}(\eta) e^{im\phi}, \quad (\text{D30b})$$

where $\ell = 0, 1, 2, \dots$, $m = -\ell, \dots, \ell$, and $n = (0, 1, 2, \dots)$ (the 0-th order element appearing only when $m = 0$). Here, the density elements are related to the potential elements through the relation

$$\nabla_{\xi, \ell, m}^2 F^{\ell mn} = D^{\ell mn}, \quad (\text{D31})$$

where

$$\nabla_{\xi, \ell, m}^2 = \frac{d}{d\xi} (\xi^2 - 1) \frac{d}{d\xi} - \ell(\ell + 1) - \frac{m^2}{\xi^2 - 1}. \quad (\text{D32})$$

We have also defined $c_\Delta(\xi, \eta) = \Delta^2 (\xi^2 - \eta^2)$. In particular, the η -components take the form $\Phi^{\ell m}(\eta) = n^{\ell m} P_\ell^m(\eta)$, where P_ℓ^m are the associated Legendre polynomials (see, e.g., [Abramowitz & Stegun 1972](#)) and

$$n^{\ell m} = \sqrt{\frac{2\ell + 1}{4\pi} \frac{(\ell - |m|)!}{(\ell + |m|)!}} (-1)^{\max(0, m)}. \quad (\text{D33})$$

is the normalization constant. The normalization comes from that of the spherical harmonics $Y_\ell^m(v, \phi)$, which can be written as $Y_\ell^m(v, \phi) = \Phi^{\ell m}(\eta) e^{im\phi}$, with $\eta = \cos v$. They are normalized to

$$\int dv d\phi \sin v |Y_\ell^m(v, \phi)|^2 = 1. \quad (\text{D34})$$

They may be called *spheroidal harmonics* in this context. Now, we define the scalar product

$$\langle \psi^{(p)}, \psi^{(q)} \rangle = -\frac{1}{4\pi G} \int d\mathbf{r} \psi^{(p)*} \nabla^2 \psi^{(q)}. \quad (\text{D35})$$

Requiring the basis elements $(\psi^{(p)}, \rho^{(p)})$ to be bi-orthogonal, i.e., satisfying the relation

$$\int d\mathbf{r} \psi^{(p)*}(\mathbf{r}) \rho^{(q)}(\mathbf{r}) = -\delta_{pq}, \quad (\text{D36})$$

means that $\{\psi^{(p)}\}_p$ should be orthonormal with respect to that scalar product.

Since the spheroidal harmonics are an orthonormal basis on the spheroid (η, ϕ) , we only have to orthonormalize the radial ξ -elements for each fixed harmonics (ℓ, m) . Thus, we should consider the radial inner product

$$\langle F^{\ell mk}, F^{\ell mn} \rangle = -\frac{1}{\Delta} \int_1^\infty d\xi F^{\ell mk}(\xi) * D^{\ell mn}(\xi). \quad (\text{D37})$$

Then, the full scalar product is related to the radial scalar product through

$$\langle \psi^{(p)}, \psi^{(q)} \rangle = \delta_{\ell^p}^{\ell^q} \delta_{m^p}^{m^q} \langle F^{\ell^p m^p n^p}, F^{\ell^q m^q n^q} \rangle. \quad (\text{D38})$$

D.1. Radial elements construction

It is preferable to choose the form of the radial elements so that the inner products are easy to compute analytically. To that purpose, we use the form obtained by [Robijn & Earn \(1996\)](#)⁶

$$F^{\ell mn}(\xi) = \frac{1}{\xi + 1} \left(\frac{\xi - 1}{\xi + 1} \right)^n. \quad (\text{D39})$$

Then, the associated density elements are given by

$$D^{\ell mn}(\xi) = \frac{(\xi - 1)^{n-1}}{(\xi + 1)^{n+3}} (C_{0,n} + C_{1,n}(\xi - 1) + C_{2,n}(\xi - 1)^2) - \frac{(\xi - 1)^{n-1}}{(\xi + 1)^{n+1}} \left(\ell(\ell + 1)(\xi - 1) + \frac{m^2}{\xi + 1} \right), \quad (\text{D40})$$

where we defined the constants

$$C_{0,n} = 8n^2, \quad (\text{D41a})$$

$$C_{1,n} = 2(1 + 2n(n + 1) - 3(2n + 1)), \quad (\text{D41b})$$

$$C_{2,n} = 2(1 - 2(n + 1)). \quad (\text{D41c})$$

Note that the $n = 0$ radial element should only be used if $m = 0$.

D.2. Computing the inner product

The inner product can be written in the form

$$\begin{aligned} -\Delta \langle F^{\ell mk}, F^{\ell mn} \rangle &= C_{0,n} I_1(k + n - 1, k + n + 4) \\ &+ C_{1,n} I_1(k + n, k + n + 4) \\ &+ C_{2,n} I_1(k + n + 1, k + n + 4) \\ &- \ell(\ell + 1) I_1(k + n, k + n + 2) \\ &- m^2 I_1(k + n - 1, k + n + 3), \end{aligned}$$

where

$$I_1(p_1, p_2) = \int_1^\infty d\xi \frac{(\xi - 1)^{p_1}}{(\xi + 1)^{p_2}}. \quad (\text{D42})$$

Following appendix B of [Robijn & Earn \(1996\)](#), we can compute these functions analytically. Indeed,

$$I_1(p_1, p_2) = B(p_1 + 1, p_2 - p_1 - 1) 2^{p_1 - p_2 + 1}, \quad (\text{D43})$$

where $B(x, y)$ is the Beta function.

⁶ Using their notations, we set $p = h = 1$.

D.3. Radial basis orthogonalization

Consider the non-orthogonal radial basis elements $\{\tilde{F}^i\}_i$. We define the Gram matrix $\mathcal{E}^{\ell m}$ by letting

$$\langle \tilde{F}^{\ell mk}, \tilde{F}^{\ell mn} \rangle = \mathcal{E}_{kn}^{\ell m}. \quad (\text{D44})$$

Then, for a given harmonics (ℓ, m) , we can write the scalar product of any radial functions G_1, G_2 as

$$\langle G_1, G_2 \rangle = G_1^T \mathcal{E}^{\ell m} G_2. \quad (\text{D45})$$

Let \mathbf{R} be the Cholesky factorization of $\mathcal{E}^{\ell m}$. Then $\mathcal{E}^{\ell m} = \mathbf{R}^T \mathbf{R}$, and we let $\mathbf{Y} = \mathbf{R}^{-1}$. It follows that

$$\mathbf{Y}^T \mathcal{E}^{\ell m} \mathbf{Y} = \mathbf{Y}^T \mathbf{R}^T \mathbf{R} \mathbf{Y} = (\mathbf{R} \mathbf{Y})^T \mathbf{R} \mathbf{Y} = \mathbf{I}. \quad (\text{D46})$$

Therefore, the columns of \mathbf{Y} form the (triangular) orthogonalization of the basis elements $\{\tilde{F}^i\}_i$, and we have

$$\tilde{F}^i = [\mathbf{Y}^T \tilde{F}]_i = \sum_{j=n_0}^i Y_{ji} \tilde{F}^j, \quad (\text{D47})$$

where $n_0 = 0$ (resp. $n_0 = 1$) if $m = 0$ (resp. $m > 0$). We drop the bar notation from now on in order not to overload notations. As an example, the Gram–Schmidt coefficients for $(\ell, m) = (0, 0)$ for $n = 0, \dots, 4$ are given by

$$\mathbf{Y} = \sqrt{\Delta} \begin{pmatrix} 2 & -\sqrt{2} & \frac{2}{\sqrt{3}} & -1 & \frac{2}{\sqrt{5}} \\ 0 & 3\sqrt{2} & -\frac{16}{\sqrt{3}} & 15 & -\frac{48}{\sqrt{5}} \\ 0 & 0 & \frac{20}{\sqrt{3}} & -45 & \frac{252}{\sqrt{5}} \\ 0 & 0 & 0 & 35 & -\frac{448}{\sqrt{5}} \\ 0 & 0 & 0 & 0 & \frac{252}{\sqrt{5}} \end{pmatrix}. \quad (\text{D48})$$

In practice, all matrix manipulations are carried out using exact integer arithmetic and symbolic computation in *Mathematica*.⁷ This allows us to obtain perfectly orthogonal basis elements with exact precision. Finally, we only need to compute the radial basis elements for $m \geq 0$ due to the $m \rightarrow -m$ symmetry.

E. LINKING ISOCHRONE SPHERE TO TOOMRE DISK

The Kuzmin–Kutuzov potential reduces to two special systems in some limits. On the one hand, in the spherical limit $a = c$, the potential reduces to the isochrone cluster ([Hénon 1960](#); [Binney & Tremaine 2008](#)), with its spherical potential given by

$$\psi(r) = -\frac{GM}{a + \sqrt{a^2 + r^2}}. \quad (\text{E49})$$

⁷ The GitHub repository, SPOCK, which contains this script, is publicly accessible at the following link: <https://github.com/KerwannTEP/SPOCK>.

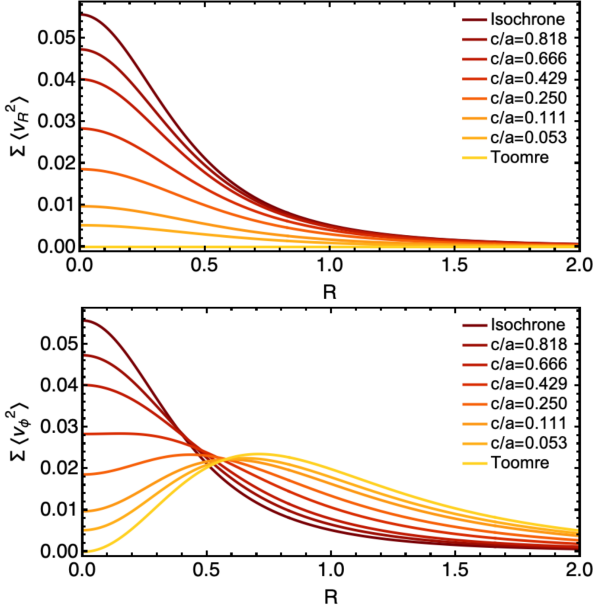


Figure E1. (Weighted) projected velocity dispersions (see, e.g., equations 3.32 and 4.17 of [DZ88](#)) of a family of Kuzmin–Kutuzov potentials, as a function of radius R . *Top panel:* $\Sigma\langle v_R^2\rangle$; *bottom panel:* $\Sigma\langle v_\phi^2\rangle$. The flattened dispersions tend toward the $m=\infty$ Toomre disk dispersions ([Miyamoto 1971](#)).

In particular, the distribution function reduces to the isotropic isochrone distribution ([DZ88](#)). On the other hand, in the flat limit $c=0$, the potential reduces to the Toomre disk ([Toomre 1963](#)), described by the potential

$$\psi(R, z) = -\frac{GM}{\sqrt{R^2 + (a + |z|)^2}}, \quad (\text{E50})$$

and the corresponding surface density

$$\Sigma(R) = \int_{-\infty}^{\infty} dz \rho(R, z) = \frac{aM}{(2\pi)(R^2 + a^2)^{3/2}}. \quad (\text{E51})$$

One can show that equation (E51) is the flat limit of the Kuzmin–Kutuzov projected surface density.

Since the Kuzmin–Kutuzov DF is a two-integral distribution, one always has $\langle v_R^2\rangle = \langle v_z^2\rangle$ ([DZ88](#)). As such, in the flat limit, both these quantities go to zero together, so that the disc is radially cold. In addition, we show in [Fig. E1](#) the transition of the projected angular velocity dispersion, $\langle v_\phi^2\rangle$, between the spherical limit and the flat limit. While the former stems from the isotropic isochrone, the latter can be obtained from the $m=\infty$ Miyamoto distribution ([Miyamoto 1971](#)), which describes a Toomre disk containing only circular orbits. This is illustrated in [Fig. E2](#), where we show the behavior of the distribution function of the angular velocity, $F(v_\phi)$, for a family of flattening parameters varying between the spherical limit and the flat limit.

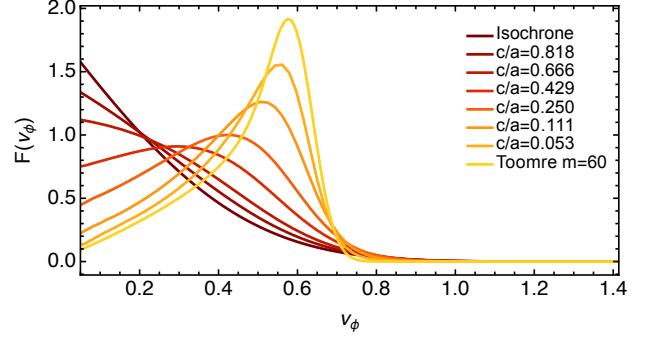


Figure E2. Distribution function of the angular velocity, $F(v_\phi)$, as a function of flattening. The distribution function tends towards that of the $m=\infty$ Toomre disk ([Miyamoto 1971](#)), which we approximate by the $m=60$ model.

F. COMPUTATION OF $\psi_{\mathbf{k}}^{(p)}(\mathbf{J})$

F.1. From angle integration to elliptic integration

We recall that the (now) bi-orthogonal potential basis elements take the form

$$\psi^{\ell mn}(\mathbf{r}) = \frac{\sqrt{4\pi G}}{\Delta} F^{\ell mn}(\xi) Y_\ell^m(v, 0) e^{im\phi}. \quad (\text{F52})$$

We let $\mathbf{k} = (k_u, k_v, k_\phi)$. The Fourier transform of these elements is given by

$$\psi_{\mathbf{k}}^{(p)}(\mathbf{J}) = \int \frac{d\theta}{(2\pi)^3} \psi^{(p)}(\mathbf{r}) e^{-i\mathbf{k}\cdot\theta}, \quad (\text{F53})$$

where each angle is integrated over $[0, 2\pi]$. Using equations (7), we can switch between angle variables and (u, v, ϕ) variables. Let us cut this integration into four parts

$$\int d\theta = \int_{\substack{p_u > 0 \\ p_v > 0}} d\theta + \int_{\substack{p_u > 0 \\ p_v < 0}} d\theta + \int_{\substack{p_u < 0 \\ p_v > 0}} d\theta + \int_{\substack{p_u < 0 \\ p_v < 0}} d\theta. \quad (\text{F54})$$

For each of these components, we can apply the bijective change of variables $\theta = (\theta_u, \theta_v, \theta_\phi) \mapsto (u, v, \phi)$, which yields

$$\int_{\substack{p_u \\ p_v}} d\theta [\dots] = \int_{p_u}^{u_1} du \int_{p_v}^{v_1} dv \int_0^{2\pi} d\phi \left| \frac{\partial(\theta_u, \theta_v, \theta_\phi)}{\partial(u, v, \phi)} \right| [\dots], \quad (\text{F55})$$

where p_u and p_v have constant signs. Furthermore, using equations (C20), the Jacobian takes the form

$$\begin{aligned} \left| \frac{\partial(\theta_u, \theta_v, \theta_\phi)}{\partial(u, v, \phi)} \right| &= \left| \frac{\partial p_u}{\partial J_u} \frac{\partial p_v}{\partial J_v} - \frac{\partial p_u}{\partial J_v} \frac{\partial p_v}{\partial J_u} \right| \\ &= \left| [J(\mathbf{w})^{-1}]^T \left| \frac{\partial p_u}{\partial E} \frac{\partial p_v}{\partial I_3} - \frac{\partial p_u}{\partial I_3} \frac{\partial p_v}{\partial E} \right| \right| \\ &= \frac{\Delta^4}{|J(\mathbf{w})|} \frac{\sinh^2 u + \sin^2 v}{|p_u p_v|}, \end{aligned} \quad (\text{F56})$$

where

$$|J(\mathbf{w})| = \left| \frac{\partial J_u}{\partial E} \frac{\partial J_v}{\partial I_3} - \frac{\partial J_u}{\partial I_3} \frac{\partial J_v}{\partial E} \right|. \quad (\text{F57})$$

It follows that the integrand of each (u, v, ϕ) -integrals is of the form

$$\begin{aligned} [\dots] &= \Psi(u, v) e^{im\phi} e^{-i\mathbf{k}\cdot\boldsymbol{\theta}}, \\ &= \Psi(u, v) e^{i(m-k_\phi)\phi} e^{-i(\alpha_{\mathbf{k}}[u] + \beta_{\mathbf{k}}[v])}, \end{aligned} \quad (\text{F58})$$

where $\Psi(u, v)$ is some function of u and v – which depends neither on the sign of p_u nor p_v – and we decomposed the angles into a u -part and a v -part using equations (7). Indeed,

$$\begin{aligned} &k_u \theta_u + k_v \theta_v + k_\phi (\theta_\phi - \phi) \\ &= \int_{u_0}^u du' \left(k_u \frac{\partial p_u}{\partial J_u} + k_v \frac{\partial p_u}{\partial J_v} + k_\phi \frac{\partial p_u}{\partial L_z} \right) \\ &+ \int_{v_0}^v dv' \left(k_u \frac{\partial p_v}{\partial J_u} + k_v \frac{\partial p_v}{\partial J_v} + k_\phi \frac{\partial p_v}{\partial L_z} \right) \\ &= \alpha_{\mathbf{k}}(u) + \beta_{\mathbf{k}}(v), \end{aligned} \quad (\text{F59})$$

where we set $\mathbf{k} = (k_u, k_v, k_\phi)$. We note that $\alpha_{\mathbf{k}}(u_1) = k_u \pi$ and $\beta_{\mathbf{k}}(v_1) = k_v \pi$. Now, carrying out the ϕ integration yields

$$\int_{\substack{p_u \\ p_v}} d\boldsymbol{\theta} [\dots] = 2\pi \delta_{k_\phi}^m \int_{u_0}^{u_1} du \int_{v_0}^{v_1} dv \Psi(u, v) e^{-i(\alpha_{\mathbf{k}} + \beta_{\mathbf{k}})}. \quad (\text{F60})$$

Because regions with p_u (resp. p_v) of opposing signs yield $\alpha_{\mathbf{k}}$ (resp. $\beta_{\mathbf{k}}$) with opposing signs, we can pair the components two-by-two to obtain an explicitly real expression

$$\oint d\boldsymbol{\theta} [\dots] = 8\pi \delta_{k_\phi}^m \int_{u_0}^{u_1} du \int_{v_0}^{v_1} dv \Psi(u, v) \cos \alpha_{\mathbf{k}} \cos \beta_{\mathbf{k}}. \quad (\text{F61})$$

F.2. Fourier transform of the basis elements

We let

$$\begin{aligned} \mathcal{J}(u, v) &= \frac{\Delta^4 (\sinh^2 u + \sin^2 v)}{|J(\mathbf{w})|} \\ &= \mathcal{J}_u(u) + \mathcal{J}_v(v). \end{aligned} \quad (\text{F62})$$

Then, combining equations (F52), (F53) and (F60) yields

$$\psi_{\mathbf{k}}^{\ell mn}(\mathbf{J}) = \frac{\sqrt{4\pi G}}{\Delta} \delta_{k_\phi}^m W_{\mathbf{k}}^{\ell mn}(\mathbf{J}), \quad (\text{F63})$$

where we defined

$$\begin{aligned} W_{\mathbf{k}}^{\ell mn}(\mathbf{J}) &= \frac{1}{\pi^2} \int_{u_0}^{u_1} \frac{du}{p_u} F^{\ell mn}(\xi) \cos(\alpha_{\mathbf{k}}) \\ &\times \int_{v_0}^{v_1} \frac{dv}{p_v} \mathcal{J}(u, v) Y_\ell^m(v, 0) \cos(\beta_{\mathbf{k}}). \end{aligned} \quad (\text{F64})$$

F.3. Computation of $\alpha_{\mathbf{k}}$ and $\beta_{\mathbf{k}}$

Let us detail an efficient method to compute $\alpha_{\mathbf{k}}$ and $\beta_{\mathbf{k}}$. Using equations (C18), (C19), (C29) and (F59), we have the relation

$$\begin{pmatrix} \alpha_{\mathbf{k}}(u) \\ \beta_{\mathbf{k}}(v) \\ k_\phi \pi \end{pmatrix}^T = \mathbf{k}^T [J(\mathbf{w})^{-1}]^T \begin{pmatrix} \int_{u_0}^u du' \frac{\partial p_u}{\partial E} & \int_{v_0}^v dv' \frac{\partial p_v}{\partial E} & 0 \\ \int_{u_0}^u du' \frac{\partial p_u}{\partial I_3} & \int_{v_0}^v dv' \frac{\partial p_v}{\partial I_3} & 0 \\ \int_{u_0}^u du' \frac{\partial p_u}{\partial L_z} & \int_{v_0}^v dv' \frac{\partial p_v}{\partial L_z} & \pi \end{pmatrix},$$

where $J(\mathbf{w})$ is the Jacobian from equation (B15). For $u = u_1$ and $v = v_1$, this reduces to

$$\begin{pmatrix} \alpha_{\mathbf{k}}(u_1) \\ \beta_{\mathbf{k}}(v_1) \\ k_\phi \pi \end{pmatrix}^T = \pi \mathbf{k}^T [J(\mathbf{w})^{-1}]^T J(\mathbf{w})^T = \pi \mathbf{k}^T. \quad (\text{F65})$$

Using the effective anomalies \tilde{u} and \tilde{v} , we can rewrite the last matrix as

$$\begin{pmatrix} \int_{-\pi/2}^{\tilde{u}} d\tilde{u}' \frac{\Delta^2 \sinh^2 u'}{\tilde{p}_u} & \int_{-\pi/2}^{\tilde{v}} d\tilde{v}' \frac{\Delta^2 \sin^2 v'}{\tilde{p}_v} & 0 \\ -\int_{-\pi/2}^{\tilde{u}} d\tilde{u}' \frac{\Delta^2}{\tilde{p}_u} & \int_{-\pi/2}^{\tilde{v}} d\tilde{v}' \frac{\Delta^2}{\tilde{p}_v} & 0 \\ -\int_{-\pi/2}^{\tilde{u}} d\tilde{u}' \frac{L_z}{\tilde{p}_u \sinh^2 u'} & -\int_{-\pi/2}^{\tilde{v}} d\tilde{v}' \frac{L_z}{\tilde{p}_v \sin^2 v'} & \pi \end{pmatrix}. \quad (\text{F66})$$

Using backward integration, we let $\alpha_{\mathbf{k}} = k_u \pi - \alpha_{\mathbf{k}}^r$ and $\beta_{\mathbf{k}} = k_v \pi - \beta_{\mathbf{k}}^r$. These new quantities read

$$\begin{pmatrix} \alpha_{\mathbf{k}}^r(u) \\ \beta_{\mathbf{k}}^r(v) \\ 0 \end{pmatrix}^T = \mathbf{k}^T [J(\mathbf{w})^{-1}]^T \begin{pmatrix} \int_u^{u_1} du' \frac{\partial p_u}{\partial E} & \int_v^{v_1} dv' \frac{\partial p_v}{\partial E} & 0 \\ \int_u^{u_1} du' \frac{\partial p_u}{\partial I_3} & \int_v^{v_1} dv' \frac{\partial p_v}{\partial I_3} & 0 \\ \int_u^{u_1} du' \frac{\partial p_u}{\partial L_z} & \int_v^{v_1} dv' \frac{\partial p_v}{\partial L_z} & 0 \end{pmatrix}.$$

Given \tilde{u} and \tilde{v} , we can rewrite the last matrix as

$$\begin{pmatrix} \int_{\tilde{u}}^{\pi/2} d\tilde{u}' \frac{\Delta^2 \sinh^2 u'}{\tilde{p}_u} & \int_{\tilde{v}}^{\pi/2} d\tilde{v}' \frac{\Delta^2 \sin^2 v'}{\tilde{p}_v} & 0 \\ -\int_{\tilde{u}}^{\pi/2} d\tilde{u}' \frac{\Delta^2}{\tilde{p}_u} & \int_{\tilde{v}}^{\pi/2} d\tilde{v}' \frac{\Delta^2}{\tilde{p}_v} & 0 \\ -\int_{\tilde{u}}^{\pi/2} d\tilde{u}' \frac{L_z}{\tilde{p}_u \sinh^2 u'} & -\int_{\tilde{v}}^{\pi/2} d\tilde{v}' \frac{L_z}{\tilde{p}_v \sin^2 v'} & 0 \end{pmatrix}. \quad (\text{F67})$$

F.4. Computation of $W_{\mathbf{k}}^{(p)}(\mathbf{J})$

Using the separability of \mathcal{J} , we have

$$W_{\mathbf{k}}^{\ell mn} = \int_{u_0}^{u_1} \frac{du}{\pi} \frac{\mathcal{J}_u F^{\ell mn} \cos(\alpha_{\mathbf{k}})}{p_u} \int_{v_0}^{v_1} \frac{dv}{\pi} \frac{Y_{\ell}^m(v, 0) \cos(\beta_{\mathbf{k}})}{p_v} \\ + \int_{u_0}^{u_1} \frac{du}{\pi} \frac{F^{\ell mn} \cos(\alpha_{\mathbf{k}})}{p_u} \int_{v_0}^{v_1} \frac{dv}{\pi} \frac{\mathcal{J}_v Y_{\ell}^m(v, 0) \cos(\beta_{\mathbf{k}})}{p_v},$$

which involves four separate one-dimensional integrals. Using effective anomalies \tilde{u} and \tilde{v} , they can be expressed using non-singular integrands as

$$W_{\mathbf{k}}^{\ell mn} = \int_{-\frac{\pi}{2}}^{\frac{\pi}{2}} \frac{d\tilde{u}}{\pi} \frac{\mathcal{J}_u F^{\ell mn} \cos(\alpha_{\mathbf{k}})}{\tilde{p}_u} \int_{-\frac{\pi}{2}}^{\frac{\pi}{2}} \frac{d\tilde{v}}{\pi} \frac{Y_{\ell}^m(v, 0) \cos(\beta_{\mathbf{k}})}{\tilde{p}_v} \\ + \int_{-\frac{\pi}{2}}^{\frac{\pi}{2}} \frac{d\tilde{u}}{\pi} \frac{F^{\ell mn} \cos(\alpha_{\mathbf{k}})}{\tilde{p}_u} \int_{-\frac{\pi}{2}}^{\frac{\pi}{2}} \frac{d\tilde{v}}{\pi} \frac{\mathcal{J}_v Y_{\ell}^m(v, 0) \cos(\beta_{\mathbf{k}})}{\tilde{p}_v},$$

where the angles $\alpha_{\mathbf{k}}$ and $\beta_{\mathbf{k}}$ can be computed on the fly following the previous section's scheme. In practice, we compute these integrals using a backward scheme.

F.5. Convergence study

Figure F1 presents the convergence of $\det(\mathbf{I} - \mathbf{M}[\omega])$ w.r.t. the sampling numbers, n_J , of the u and v action variables in equation (15). The action space integral itself is performed by transforming the infinite domain $[0, \infty) \times [0, \infty) \times (-\infty, \infty)$ into the compact domain $[0, \pi/2) \times [0, \pi/2) \times (-\pi/2, \pi/2)$ by using the change of variables

$$J_i \mapsto \tilde{J}_i = \tan^{-1} \left(\frac{J_i}{\sqrt{GM(a+c)}} \right), \quad (\text{F68})$$

for each action variables. The integration itself is then carried out using mid-point sampling. From this figure we assume convergence for $n_J = 256$, which we take for our computation. As for L_z , we use in this paper $n_{L_z} = 128$.

G. INTRODUCING ROTATION

G.1. Distribution function: Lynden-Bell daemon

Using the Lynden-Bell parametrization (Lynden-Bell 1960), the density profile of the cluster does not depend on the rotation parameter α_r . Its derivatives w.r.t. the action variables read

$$\frac{\partial F_{\text{rot}}}{\partial J_u} = \frac{\partial F}{\partial J_u} (1 + \alpha_r \text{sgn}[L_z]), \quad (\text{G69a})$$

$$\frac{\partial F_{\text{rot}}}{\partial J_v} = \frac{\partial F}{\partial J_v} (1 + \alpha_r \text{sgn}[L_z]), \quad (\text{G69b})$$

$$\frac{\partial F_{\text{rot}}}{\partial L_z} = \frac{\partial F}{\partial L_z} (1 + \alpha_r \text{sgn}[L_z]) + 2\alpha_r F(\mathbf{J}) \delta_{\text{D}}(L_z), \quad (\text{G69c})$$

where $F(\mathbf{J}) = F(E[J_u, J_v, L_z], L_z)$. Therefore, the computation of the response matrix requires slight modifications.

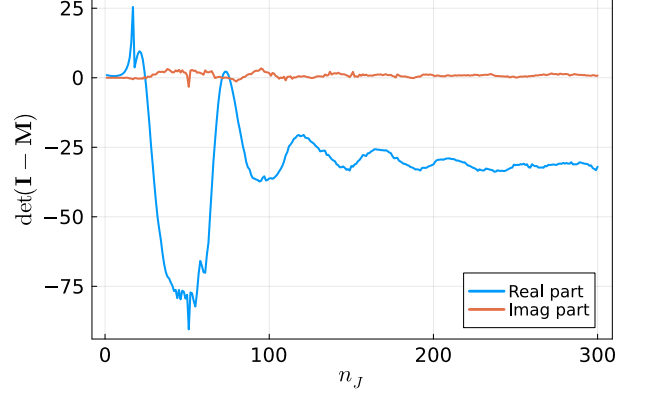


Figure F1. Convergence of $\det(\mathbf{I} - \mathbf{M}[\omega])$, for $m = 2$, w.r.t. the sampling numbers, n_J , of the u and v action variables. The plotted value is taken to be the average of a sampling number of the L_z action of 80 and of 81 – to increase convergence speed – while we set $a = 0.85$ and $\omega = 0.01i$.

Most notably, one must take into account the Dirac delta contribution, whose implementation should be performed carefully. Indeed, the third frequency Ω_z has two distinct left-sided and right-sided limits at $L_z \rightarrow 0$. We can remedy this issue by recalling that integration over δ_{D} should be understood as the limit

$$\int_{-\infty}^{\infty} dx g(x) \delta_{\text{D}}(x) = \lim_{a \rightarrow 0^+} \int_{-\infty}^{\infty} dx g(x) \eta_a(x). \quad (\text{G70})$$

over a set of functions $g(x)$. Here, $\eta_a \rightarrow \delta_{\text{D}}$ converges in the distributional sense, with $\eta_a(x) = \eta(x/a)/a$ where η is an even function integrating to 1. Then

$$\int_{-\infty}^{\infty} dx g(x) \eta_a(x) = \int_{-\infty}^{\infty} dy g(ay) \eta(y) \quad (\text{G71}) \\ = \int_{-\infty}^0 dy g(ay) \eta(y) + \int_0^{\infty} dy g(ay) \eta(y) \\ \rightarrow \int_{-\infty}^0 dy g(0^-) \eta(y) + \int_0^{\infty} dy g(0^+) \eta(y).$$

Since η is even and integrates to 1, it follows that

$$\int_{-\infty}^{\infty} dx g(x) \delta_{\text{D}}(x) = \frac{g(0^+) + g(0^-)}{2}. \quad (\text{G72})$$

G.2. Response matrix

The rotational response matrix elements can be decomposed into two contributions

$$M_{pq}^m(\omega) = M_{pq}^{m,a}[\omega] + \alpha_r (M_{pq}^{m,b}[\omega] + M_{pq}^{m,c}[\omega]), \quad (\text{G73})$$

where

$$M_{pq}^{m,a}(\omega) = \frac{32\pi^4 G}{\Delta^2} \sum_{\substack{k_u, k_v \\ \ell^p + m + k_v \text{ even} \\ \ell^q + m + k_v \text{ even}}} \int d\mathbf{J} \frac{\mathbf{k} \cdot \partial F / \partial \mathbf{J}}{\omega - \mathbf{k} \cdot \boldsymbol{\Omega}} W_{\mathbf{k}}^{(p)} W_{\mathbf{k}}^{(q)},$$

$$M_{pq}^{m,b}(\omega) = \frac{32\pi^4 G}{\Delta^2} \sum_{\substack{k_u, k_v \\ \ell^p + m + k_v \text{ even} \\ \ell^q + m + k_v \text{ even}}} \int d\mathbf{J} \frac{\mathbf{k} \cdot \partial F / \partial \mathbf{J}}{\omega - \mathbf{k} \cdot \boldsymbol{\Omega}} \text{sgn}[L_z] W_{\mathbf{k}}^{(p)} W_{\mathbf{k}}^{(q)},$$

$$M_{pq}^{m,c}(\omega) = \frac{64\pi^4 G}{\Delta^2} \sum_{\substack{k_u, k_v \\ \ell^p + m + k_v \text{ even} \\ \ell^q + m + k_v \text{ even}}} \int d\mathbf{J} \frac{mF(\mathbf{J})}{\omega - \mathbf{k} \cdot \boldsymbol{\Omega}} \delta_D(L_z) W_{\mathbf{k}}^{(p)} W_{\mathbf{k}}^{(q)}.$$

Using the Dirac delta function, we can reduce the 3D integral to a 2D integral by applying equation (G72)

$$M_{pq}^{m,c}(\omega) = \frac{64\pi^4 G}{\Delta^2} \sum_{\substack{k_u, k_v \\ \ell^p + m + k_v \text{ even} \\ \ell^q + m + k_v \text{ even}}} \int dJ_u dJ_v \left[\frac{mF(\mathbf{J})}{\omega - \mathbf{k} \cdot \boldsymbol{\Omega}} W_{\mathbf{k}}^{(p)} W_{\mathbf{k}}^{(q)} \right]_s,$$

where we defined the symmetric central value

$$[g(\mathbf{J})]_s = \lim_{\delta L_z \rightarrow 0^+} \frac{g(J_u, J_v, \delta L_z) + g(J_u, J_v, -\delta L_z)}{2}.$$

H. Z-SLICE OF THE BENDING MODE'S SHAPE

As a complement to Fig. 7, let us highlight the impact of rotation of the shape of bending mode by representing a z -slice of the mode in Fig. H1. Rotation appears to have a small, but real impact on the mode's shape.

I. ANALYTIC CONTINUATION

Let us consider a function $g(z)$, for which we have access to a set of $2N + 1$ values $\{g_k\}_k = \{g(z_k)\}_k$ over a sampling $\{z_k\}_k$. Let us consider the approximation

$$g(z) = \frac{P(z)}{Q(z)} = \frac{\sum_{i=0}^N a_i z^i}{1 + \sum_{i=1}^N b_i z^i}. \quad (\text{I75})$$

Although there exist recursive relations to compute the coefficients of P and Q (see, e.g., [Stoer & Bulirsch 1980](#)), one can directly compute those using linear algebra. Indeed, let us define $\mathbf{c} = (a_0, \dots, a_N, b_1, \dots, b_N)$, $\mathbf{g} = (g_1, \dots, g_{2N+1})$ and the matrix \mathbf{A} such that

$$A_{kj} = \begin{cases} z_k^{j-1}, & \text{if } j = 1, \dots, N+1, \\ -g_k z_k^{j-N-1}, & \text{otherwise.} \end{cases} \quad (\text{I76})$$

Then, one can recover the coefficients \mathbf{c} by solving the equation

$$\mathbf{A} \mathbf{c} = \mathbf{g}. \quad (\text{I77})$$

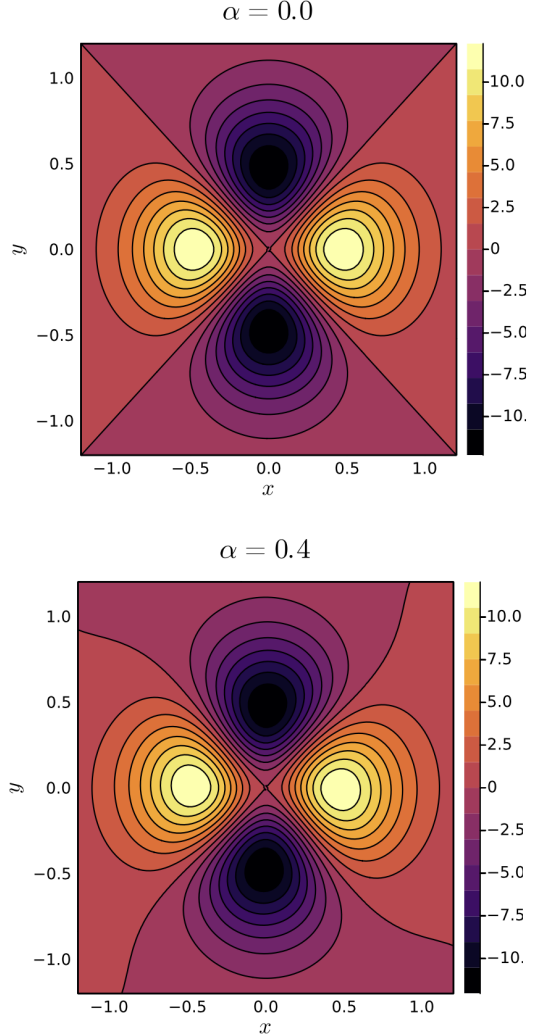


Figure H1. Slice $z = 0.1$ of the $m = 2$ density modes of a $a = 0.9$ cluster, for the non-rotating bending mode ($\alpha = 0$, top panel, see Fig. 3), and a rotating bending mode ($\alpha = 0.4$, bottom panel, see Fig. 7). Rotation only weakly impacts the shape of the mode.

J. MACLAURIN SPHEROID

Self-gravitating fluids with uniform rotation are known to possess flattened equilibrium states: the so-called Maclaurin spheroids ([Chandrasekhar 1969](#)). Their angular momentum, L , and energy, E , read as a function of eccentricity

$$\hat{L} = \frac{\sqrt{6}}{5} \frac{(\cos \gamma)^{-\frac{1}{6}}}{\sin \gamma} \sqrt{(1 + 2 \cos^2 \gamma) \frac{\gamma}{\sin \gamma} - 3 \cos \gamma}, \quad (\text{J78a})$$

$$\hat{E} = -\frac{3}{10} \frac{(\cos \gamma)^{\frac{1}{3}}}{\sin^2 \gamma} \left[(1 - 4 \cos^2 \gamma) \frac{\gamma}{\sin \gamma} + 3 \cos \gamma \right], \quad (\text{J78b})$$

where $e = \sin \gamma = \sqrt{1 - c^2/a^2}$, $\bar{a} = (a^2 c)^{1/3}$, $\hat{L} = L/\sqrt{GM^3 \bar{a}}$ and $\hat{E} = -aE/(GM^2)$. Therefore, it follows that its spin parameter is given by

$$\lambda_r = \hat{L} \sqrt{\hat{E}} \sqrt{\bar{a}/a}. \quad (\text{J79})$$

K. SUBDOMINANT BENDING AND BAR MODES

Let us extend the growth rates of the bending and bar-growing modes into their subdominant branches in Fig. K1. The bending mode approaches zero for the maximally rotating cluster, while the bar-growing modes exhibit the opposite behavior. This establishes a threshold at which highly flattened clusters are the least prone to instability. For highly flattened clusters, we note the presence of multiple bar modes – whose shapes are given in Fig. K2 – whose hierarchy appears to depend on the rotation of the cluster.

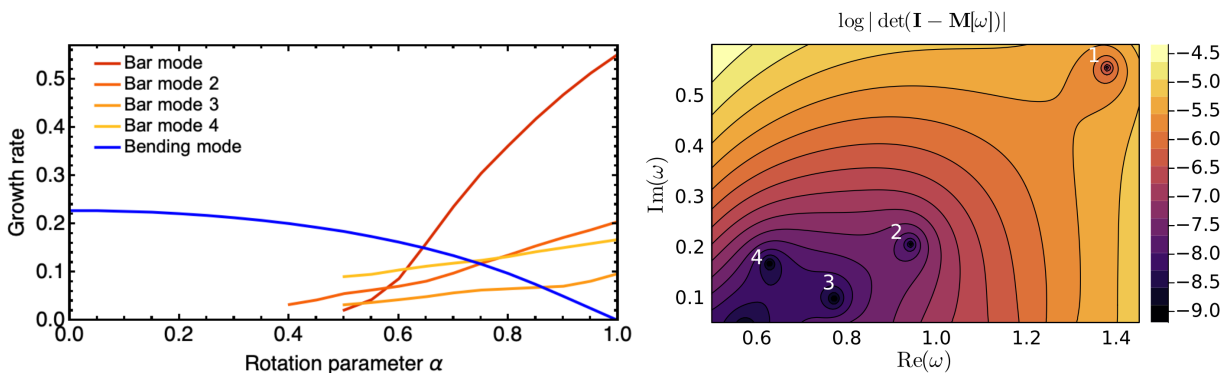


Figure K1. *Left panel:* Growth rate of the dominant bending modes (in blue) and bar-growing mode (in red), as a function of rotation, for a clusters with flattening ratio $c/a=0.11$. We used the parameters $\ell_{\max}=30$ and $n_{\max}=20$. The bending mode is dominant for slowly rotating clusters, with a growth rate which goes to 0 for the maximally rotating cluster. *Right panel:* Location in frequency space of the four bar modes of the maximally rotating cluster.

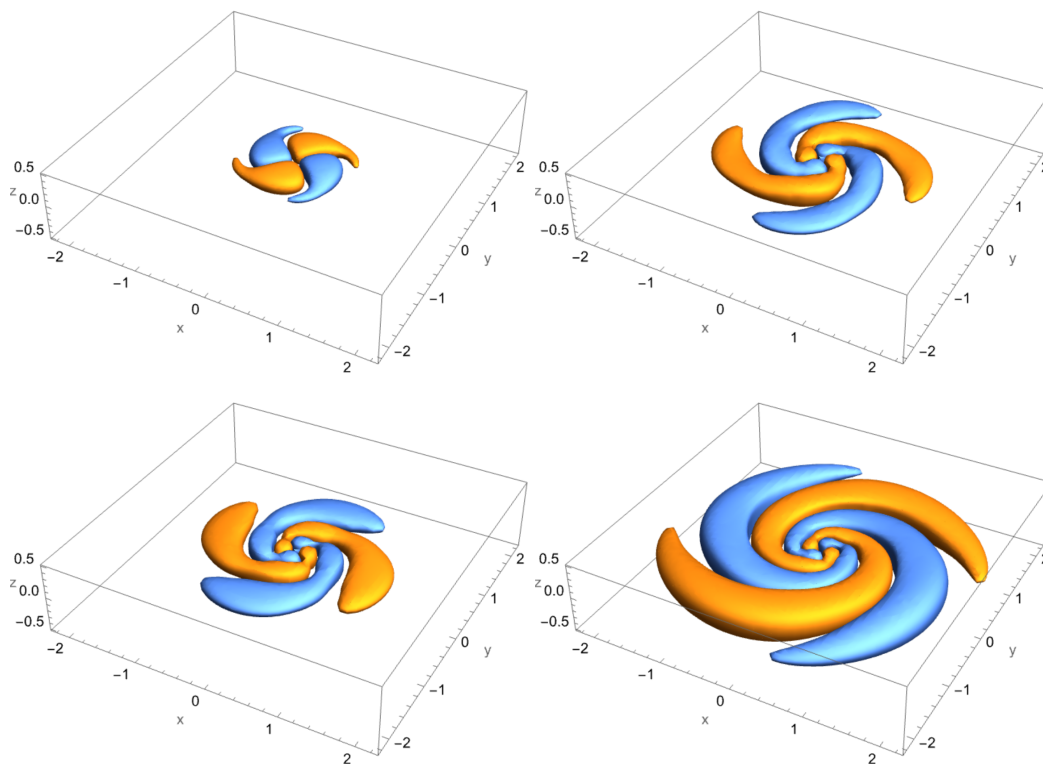


Figure K2. Shapes of the maximally rotating modes obtained in Fig. K1. *Top left panel:* bar mode 1. *Top right panel:* bar mode 2. *Bottom left panel:* bar mode 3. *Bottom right panel:* bar mode 4. The modes exhibit a spiral structure characteristic of the rapidly growing bar modes in the flattened Kuzmin–Kutuzov cluster, with each successive subdominant modes appearing increasingly wound and larger scale.